2021

Improving patient-specific assessments of regional aortic mechanics via quantitative magnetic resonance imaging with early applications in patients at elevated risk for thoracic aortopathy

Patrick A. Jones
Virginia Commonwealth University

IMPROVING PATIENT-SPECIFIC ASSESSMENTS OF REGIONAL AORTIC MECHANICS VIA QUANTITATIVE MAGNETIC RESONANCE IMAGING WITH EARLY APPLICATIONS IN PATIENTS AT ELEVATED RISK FOR THORACIC AORTOPATHY

A thesis submitted in partial fulfillment of the requirements for the degree of Master of Science in Biomedical Engineering at Virginia Commonwealth University.

By

PATRICK A. JONES
B.S. Biomedical Engineering, Virginia Commonwealth University, 2019

Director: John S. Wilson, M.D., Ph.D.
Assistant Professor, Department of Biomedical Engineering and Pauley Heart Center
Director, Cardiovascular Mechanics and Imaging Laboratory

Virginia Commonwealth University
Richmond, Virginia
May 2021

Acknowledgement

I would first like to thank my thesis advisor, Dr. John Wilson in the Department of Biomedical Engineering. Thank you for all the support over these past two years. Graduate school during a global pandemic was not what I had in mind when I started, but you helped me to stay on track despite all the hurdles we faced carrying out this research. From tissue biomechanics and MRI methods to the general research process, I have learned so much from you that I plan to take forward with me in my future career as a physician scientist.

Next, I would like to thank Dr. Jennifer Jordan in the Department of Biomedical Engineering and Dr. Uyen Truong in the Department of Pediatrics for serving on my committee. I appreciate you both for your willingness to work with me and to provide valuable feedback about my research. Additionally, I would like to thank you Dr. Truong for all your efforts to get this research project off the ground and for showing me the ins and outs of 4D flow MRI acquisition.

To the other members of the Cardiovascular Mechanics and Imaging Laboratory, thank you for the help with manual mask segmentations, the thoughtful questions during meetings, and the general feedback about my work. I wish you all the best and am looking forward to seeing your projects once they are completed.

I would also like to thank my family. To my mom Susan and dad Stephen, thank you for the continued love and support. You have always been my biggest fans and have encouraged me endlessly to pursue my goals. To my brother Griffin and sister Meghan, thank you for the emotional support and for pulling me away from my work on occasion to have some fun.

Lastly, to my wonderful girlfriend Jessie, thank you for being my rock throughout this process, even when you were 800 miles away. From our walks through Byrd park to evening phone calls, you have kept me sane throughout this journey and I am beyond grateful.

Table of Contents

List of Tables

List of Figures

List of Abbreviations

AVI	Aorto-vertebral interface
CoV	Coefficient of variation
CT	Computed tomography
CVD	Cardiovascular disease
DAA	Distal aortic arch
DENSE	Displacement encoded with stimulate echoes
DTA	Descending thoracic aorta
Ecc	Circumferential strain
ECG	Electrocardiogram
Erc	Shear strain
Err	Radial strain
IAA	Infrarenal thoracic aorta
IRB	Institutional review board
LPA	Left pulmonary artery
MRI	Magnetic resonance imaging
NCS	Normalized circumferential strain
NRS	Normalized radial strain
NSS	Normalized shear strain
PC-MRI	Phase-contrast magnetic resonance imaging
PDA	Proximal descending aorta
SD	Standard deviation
SENC-MRI	Strain-encoded magnetic resonance imaging
SVD	Singular value decomposition
TDI	Tissue doppler imaging
TPV	Tracked position vectors
WNS	Wall normal stress
WSS	Wall shear stress

Abstract

IMPROVING PATIENT-SPECIFIC ASSESSMENTS OF REGIONAL AORTIC MECHANICS VIA QUANTITATIVE MAGNETIC RESONANCE IMAGING WITH EARLY APPLICATIONS IN PATIENTS AT ELEVATED RISK FOR THORACIC AORTOPATHY

Patrick A. Jones

A thesis submitted in partial fulfillment of the requirements for the degree of Master of Science in Biomedical Engineering at Virginia Commonwealth University.

Director: John S. Wilson, M.D., Ph.D.
Assistant Professor, Department of Biomedical Engineering and Pauley Heart Center
Director, Cardiovascular Mechanics and Imaging Laboratory

Virginia Commonwealth University
Richmond, Virginia
May 2021

Unstable aortic aneurysms and dissections are serious cardiovascular conditions associated with high mortality. The current gold standards for assessment of stability, however, rely on simple geometric measurements, like cross-sectional area or increased diameter between follow-up scans, and fail to incorporate information about underlying aortic mechanics. Displacement encoding with stimulated echoes (DENSE) magnetic resonance imaging (MRI) has been used previously to determine heterogeneous circumferential strain patterns in the aortas of healthy volunteers. Here, I introduce technical improvements to DENSE aortic analysis and early pilot application in patients at higher risk for the development of aortopathies. Modifications to the DENSE aortic postprocessing method involving the separate spatial smoothing of the inner and outer layers of

the aortic wall allowed for the preservation of radial and shear strains without impacting circumferential strain calculations. The implementation of a semiautomatic segmentation approach utilizing the intrinsic kinematic information provided by DENSE MRI reduced lengthy post-processing times while generating circumferential strain distributions with good agreement to a manually generated benchmark. Finally, a new analysis pipeline for the combined use and spatial correlation of 4D phase-contrast MRI alongside DENSE MRI to quantify both regional fluid and solid mechanics in the descending aorta is explored in a limited pilot study.

1 Introduction

The burden of cardiovascular disease (CVD) in the United States is substantial and growing, with over 40% of Americans estimated to have some form of CVD in 2015 with projections of that number growing to 132 million people, or over 45% of the population by 2035 [1]. In addition to the detrimental impacts on individual health, CVD was estimated to have a total economic cost of $555 billion in 2015, a number projected to more than double by 2035 [1]. Some of the most prevalent forms of CVD or CVD risk factors, including hypertension and hyperlipidemia, are also risk factors for developing more severe pathologies [2]. With an incidence of 3.5-15.0 per 100,000 patients each year, aortic aneurysm or dissection is associated with particularly high mortality in patients who develop these vascular pathologies, with mortality rates of up to 17-27% for acute dissection depending on aorta location and availability of intervention [3]. However, even among patients that do receive timely medical intervention for these conditions, perioperative mortality rates of open vascular surgery and endovascular aortic repair (EVAR) demonstrate the importance of accurately assessing the stability of the vessel wall before electing to perform surgery [4]. The current gold standard for rupture risk assessment is based on aortic cross-sectional size alone and does not adequately differentiate between risk of rupture and baseline surgery risk except in larger aneurysms, necessitating the development of new methods for quantifying patient-specific vascular risk [5, 6].

Over the past several decades, imaging methods for noninvasive assessment of cardiovascular structure and function have become the essential clinical tools for diagnosis and treatment of patients with CVD. Beginning with the first clinical applications of ultrasound echocardiography in the 1950s to assess mitral stenosis and followed by developments in the 1970s

and 1980s of computed tomography (CT) imaging and magnetic resonance imaging (MRI) to assess cardiac morphology and myocardial tissue characterization, these imaging techniques have radically changed how CVD and aortopathies in particular are diagnosed and treated clinically [7, 8, 9]. More recently, developments within these imaging modalities to better assess the function of the tissue or organ in addition to the morphology have become the gold standard for diagnosis of cardiovascular disease. Continued improvements to these imaging techniques will benefit the diagnostics, treatment planning, and follow-up assessment of medical and surgical interventions in patients with CVD to reduce the mortality for patients living with chronic disease or at risk of developing acute conditions, including aneurysms and dissections.

Echocardiography has long been the standard of care for diagnosing CVD from any of several relevant clinical indicators including left ventricular ejection fraction, cardiac hypertrophy, and valvular morphological defects [10]. Doppler ultrasound takes this one step further, allowing for the determination of abnormal blood flow patterns in the heart and vessels to diagnose a range of conditions including valvular regurgitation, atherosclerosis, and thrombosis [11]. These findings are clinically correlated with disease progression or general outcomes but fail to describe specific changes within the myocardial and vascular tissues that may contribute to disease progression. For example, assessing the deformation of the left ventricle in patients with heart failure has been shown to better predict mortality in patients compared to measuring ejection fraction alone [12]. It is likely that in other disease states, such as in cases of assessing aortic aneurysm stability, the quantification of the mechanics of the vascular tissues would advance the understanding of a patient's underlying pathophysiology and risk of adverse outcome. To fully understand the progression of cardiovascular disease, it is therefore necessary to accurately

quantify the mechanical forces being applied to or by the tissues *in situ* to determine how mechanical behavior changes with the development and progression of disease.

1.1 Cardiovascular Biomechanics

Biomechanics, or the application of classical mechanics to solve biological problems, is fundamentally concerned with quantifying the mechanical environments of living tissues to understand their structure and function [13]. Mechanobiology describes how cells and tissues change their behavior, such as through signaling, transcription modification, or protein translational modification in response to physical forces and changes to the mechanical environment [14]. There is a constant dynamic relationship between how cells and tissues experience physical stimulation and in turn modify how they interact with their external environment due to these physical cues. In the aorta, for example, the elasticity of the vessel serves to convert pulsatile flow from the left ventricle into steady flow as blood moves through the vasculature [15]. Disruptions to normal fluid mechanics such as elevated blood pressure results in elevated stress which can damage vascular tissues, resulting in loss of normal aortic remodeling leading to accelerated arterial stiffening [16]. A better quantification of the mechanics of cardiovascular disease in an individual can lead to improved diagnosis and prognosis, and to better guide the interventions for that individual patient.

To adequately frame a biomechanics problem, it is necessary to determine the morphology or geometry of the material or tissue, the mechanical properties of the material, the basic governing laws of the system, and the environment surrounding the material to determine acceptable boundary conditions [13]. While tissue and organ morphology in patients can be assessed using

imaging, ascertaining the precise mechanical properties of the tissue in the native environment is generally not possible.

One way to get around this limitation is through studying the deformation of a tissue instead. Various imaging techniques introduced in the next section can be used to directly measure tissue deformation, that can in turn be used to calculate mechanical strain in that tissue. One-dimensional strain is defined by equation 1.1,

$$\varepsilon = \frac{L - L_0}{L_0} \tag{1.1}$$

where strain (ε) is equal to the change in length with respect to the original reference length between two points. Hooke's law states that

$$\sigma = E * \varepsilon \tag{1.2}$$

where σ is stress, E is the stiffness of the material, and ε is the strain, demonstrating the direct relationship between measured deformation and material stress for a perfectly elastic body. The strain relationship shown in equation 1.1 is expandable to 2D and 3D as well.

However, most biological tissues including the wall of a blood vessel exhibit nonlinear stress-strain relationships for the magnitudes of strain found *in situ* and are better described by exponential equations, such as the unified stress-strain equation for uniaxial stretch introduced by Fung et al. [17],

$$T = \beta\left[e^{\alpha(\lambda-1)} - 1 - \alpha(\lambda - 1)\right] + E(\lambda - 1) \tag{1.3}$$

where T is stress, λ is the stretch ratio at zero-stress state, E is the stiffness, and α and β are experimentally derived constants. While not the emphasis of this work, obtaining the strain behavior of the aorta wall *in situ* can be applied to inverse mechanics problems [18], or related to directly to stress by equation 1.3 with the inclusion of constants specific to the tissue.

As outlined in Humphrey and O'Rourke [19], the Green strain is a measure of deformation that is unaffected by rigid-body motion, which is beneficial for looking at strains in tissues that are also undergoing bulk motion such as the heart translating through 3D space during contraction. The Green strain can be calculated for 2D using equation 1.4,

$$\boldsymbol{E} = \frac{1}{2}(\boldsymbol{F}^T \cdot \boldsymbol{F} - \boldsymbol{I}) \tag{1.4}$$

where $\boldsymbol{I}$ is the 2x2 identity matrix, and $\boldsymbol{F}$ is the deformation gradient matrix shown in equation 1.5.

$$\boldsymbol{F} = \begin{bmatrix} \frac{\partial x}{\partial X} & \frac{\partial x}{\partial Y} \\ \frac{\partial y}{\partial X} & \frac{\partial y}{\partial Y} \end{bmatrix} \tag{1.5}$$

For finding the relevant 2D strains for a cross-section of a cylindrical body, this 2D *xy*-coordinate system can be converted to radial circumferential coordinates using rotation matrices as demonstrated in Wilson et al. [20] to yield circumferential, radial, and radial-circumferential shear strain as shown in Figure 1.1. Therefore, the strain can be computed directly from the deformation measured *in vivo* using a variety of imaging methods outlined in the next section.

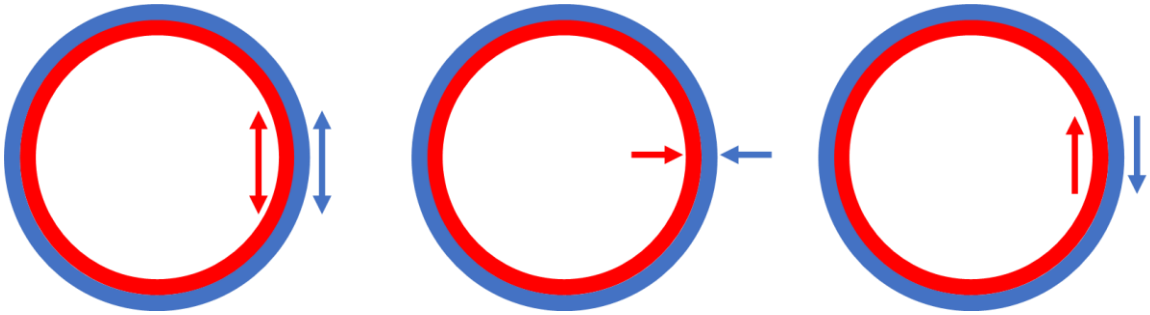

Figure 1.1: Diagram showing relative movement of inner (red) and outer (blue) layers of a hollow cylinder cross-section, demonstrating circumferential strain (left), radial strain (middle), and radial-circumferential shear strain (right).

1.2 Cardiovascular Strain Imaging

Clinically, ultrasound and magnetic resonance imaging are most often used to evaluate tissue strain in the heart, and some of these methods have been modified to measure strain in large vessels as well. The two most common ultrasound methods for characterization of tissue strain include echocardiographic strain and strain-rate imaging derived from Doppler ultrasound images and strain imaging from 2D speckle-tracking techniques [21]. Tissue Doppler imaging (TDI) involves sampling velocity measurements in a 2D slice to yield a spatial velocity gradient, where strain rate between two points can be approximated as,

$$SR \approx \frac{V_2 - V_1}{d} * cos\theta, \tag{1.6}$$

where V_1 and V_2 are the velocities measured at two points, d is the distance between the two points, and θ is the angle between the ultrasound beam and the direction of tissue movement [22]. These strain rates can then be used to calculate strain between those points by integrating over the sampling period [21]. There are some drawbacks of this method for calculating tissue strain, however. In addition to the high interobserver variability arising from the effect of transducer alignment to tissue displacement, the velocities used in this calculation are 1D measurements in the direction of ultrasound wave propagation, and therefore do not perform well when describing complex deformations in multiple dimensions such as those that occur in the myocardium or the aortic arch [22].

An alternative ultrasound technique for measuring tissue strain in 2D is non-Doppler speckle-tracking ultrasound. Speckles are natural acoustic markers that occur in the ultrasound window in two dimensions and are distributed throughout a given tissue [21, 23]. These speckles can be tracked between frames over time, giving a displacement in two dimensions of each individual speckle that remains in the plane through subsequent timepoints. The velocity field is

then calculated based upon these frame-by-frame displacements and the framerate, thereby allowing for the generation of a velocity field in 2D for determination of strain rate and strain as previously discussed [23].

Advantages of this method over Doppler ultrasound include lower intraobserver variability and lower noise sensitivity, as well as the ability to resolve velocity components in the longitudinal and transverse directions simultaneously, allowing quantification of more complex multi-dimensional strains such as those that occur in the myocardium [23, 24]. However, a drawback of this speckle-tracking method is the possibility for a given tracked speckle to move out of the 2D ultrasound imaging plane during data collection. To correct for this, most commercial software relies on assumptions that the neighboring speckles have the same velocities as those disappearing from the plane, but this can lead to discrepancies if there is a high heterogeneity in strain in a specific region [23]. Doppler and speckle-tracking ultrasound allow for direct mechanical measurements in addition to quantifying morphological features, but lower anatomical resolution and limitations resolving strains in tissues with complex movements make it difficult to accurately quantify small strain heterogeneities in cardiovascular tissue.

Cine MRI is an alternative imaging modality that can generate spatial and temporal information from cardiovascular tissues with high resolution in large imaging windows, yielding accurate strain assessments in a specific structure via tracking or directly measuring tissue displacements while retaining the ability to assess contribution of surrounding anatomy on those mechanics. In cardiovascular MRI, several approaches have been explored for determining global and local strains in the left ventricle, with some limited applications in smaller anatomic structures such as the right ventricle and aorta. Myocardial feature tracking is one commonly available commercial method that allows for the determination of global and regional strains from the

motion of distinct visual features, such as border contours between the myocardium and ventricular cavity [25, 26]. The displacements of these specific features are tracked over time and combined to generate myocardial tissue strains in the imaging plane [25]. While this method performs well against the clinical gold stand of speckle tracking echocardiography for quantification of global longitudinal and circumferential strains, the dependence on tissue boundary tracking results in unreliable local strain values that prevent the resolution of small focal heterogeneities that may precede larger global changes in disease development [27]. Other disadvantages of MRI feature tracking include sensitivity to through-plane motion resulting in dropping of tracked features from the image plane, and an inability to resolve displacements smaller than the size of the pixels used in the images [28].

Magnetization tagging, or grid tagging, is a method that allows for the measurement of strain throughout a structure of interest by measuring the displacement of a regularly spaced grid pattern overlayed onto the image, as opposed to feature tracking methods that rely on tissue boundaries alone [29, 28]. Radiofrequency pulses are applied perpendicular to the imaging plane, repeating regularly in two spatial directions to create a grid pattern of low signal in the imaging plane prior to the image acquisition period [30]. The displacement of these grid patterns is tracked over time and used to calculate strain for all grid segments overlaying a structure, such as the left ventricular wall [30]. Myocardial tagging has become a commonly accepted reference standard for MR strain quantification due to this advantage [31], but limitations on the minimum spacing of tagging lines while maintaining sufficient image signal prevents the imaging of thinner walled structures such as the right ventricle or aorta [30, 32].

Strain-encoded (SENC) MRI is another tagging-based method for measuring tissue strain but differs from grid tagging in the direction of motion measured by the technique. Rather than

applying grids in orthogonal directions to the imaging plane, SENC applies tags in a series of planes parallel to the imaging plane [33]. As a tissue moves in the through-plane direction, the tagged planes compress together or spread apart, causing a shift in the peak spectrum location in k-space which can be used to measure regional strain in the through-plane direction [33]. SENC shows good agreement with myocardial tagging methods for measuring left ventricular strain with low interobserver variability, but the ability to only measure through plane motion limits the technique to single dimension strain measurements for each acquisition [34]. This limitation also complicates image positioning for scans of thinner tissues or in tissues with a high curvature in the through-plane direction, such as measuring circumferential strain in the aorta. In general, standard myocardial ultrasound strain imaging methods and tracking-based (via physical features or tags) MR imaging sequences are insufficient to measure strain heterogeneities in thin structures like the aortic wall.

An alternative approach to strain imaging with MR is to directly measure the kinematics of tissues on a voxel-wise level rather than using indirect measurements of feature or grid displacements. Phase-contrast (PC) MRI measures voxel-wise velocities to calculate strain profiles, with similar advantages to Doppler ultrasound but with the added ability to measure this displacement in multiple directions simultaneously. In addition to uses in measuring blood flow velocities, PC-MRI has been used to measure the velocity of the myocardial tissue during contraction in three dimensions, allowing for the determination of motion heterogeneities between discrete circumferential regions the ventricular wall [35, 36].

PC-MRI has also been expanded to imaging of the aortic wall, where fields of velocity vectors from the PC-MRI sequence were segmented into circumferential sectors overlaying the aortic wall, and sector velocity vectors were assigned as the average of all enclosed velocity values

for that given sector [37]. The sector starting positions were determined and velocities were measured over time to determine the stepwise displacement of the center of each sector using a forward-backward time integration approach throughout the image acquisition period. Validation in phantom and *in-vivo* porcine thoracic aortic models of PC-MRI displacement calculations against embedded imaging marker motion in the vessel wall have shown good agreement [37, 38]. However, lengthy scan times for PC-MRI can introduce errors due to temporal variations in tissue physiology and any errors in velocity measurements are propagated through the integration of pixel-wise velocity measurements, especially in the presence of through-plane motion which notably occurs in the aortic arch from the contractile pull of the myocardium [29, 39].

Displacement encoding with stimulated echoes (DENSE) MRI is a sequence developed for functional cardiac measurements of strain through direct tracking of tissue displacement from phase data. As outlined by Aletras [40], encoding phase proportional to tissue displacement is done through a series of radiofrequency and paired magnetic gradient pulses that induce phase dispersion in the selected direction for a slice. The second of the paired directional magnetization gradients subsequently undoes previously induced phase dispersion for all stationary spins but does not fully zero the phase for any spins that had displaced between the time of the two gradients. The remaining phase from voxels representing moving tissue is captured during image acquisition and related to displacement with equation 1.7,

$$\varphi = \gamma_H * G_x * t_{enc} * \Delta x \tag{1.7}$$

where φ is the accumulated phase captured during image acquisition, γ_H is the gyromagnetic ratio for hydrogen, G_x is the amplitude of the matched gradient pulses in the *x*-direction, t_{enc} is the encoding time duration, and Δx is the displacement in the *x*-direction, though this process is the same for all three principal dimensions. The imaging sequence is again repeated using different

amplitude gradient pulses to remove phase contributions common to both timepoints, and the differences in phase between the two acquired images is used to calculate the tissue displacement using equation 1.8,

$$\Delta\varphi = \gamma_H * (G_x - G_x^*) * t_{enc} * \Delta x \quad (1.8)$$

where G_x^* is the amplitude of the second image gradient pulse pair.

The primary advantage of DENSE is that it directly encodes the displacement into the image, rather than through processing velocity information like PC-MRI. This avoids the problem of error propagation when integrating those velocities. Also, by using information directly encoded in the image signal to determine displacement rather than only spatial voxel information like feature tracking, it is possible to resolve partial voxel displacements and therefore more accurate strains with higher spatial resolution throughout the bulk of a tissue compared to feature tracking or grid-tagging [41, 42]. In addition to spatial resolution advantages over feature tracking and magnetization tagging, DENSE also has a high level of reproducibility in both phantom trials and human subject studies for global and regional measurements of strain in the left ventricle [43, 44].

While successfully used in myocardial strain imaging, the application of DENSE to measuring aortic wall strain has only been explored more recently. It has been shown that even in the aortic wall that measures a few millimeters thick, DENSE can resolve circumferential strain heterogeneities on a regional basis [20]. In a healthy patient population, DENSE also showed the ability to discern normal aortic mechanics at different axial aorta locations and how these normal distributions differed with patient demographics [45]. Some limitations of DENSE for aortic imaging include long scan times, low signal to noise ratio, and a reliance on time-intensive manual segmentation that limits both intraobserver and interobserver repeatability for aortic cross-sectional strain maps.

In this body of work, I will be detailing my recent efforts to improve the use of DENSE MRI in analyzing aortic mechanics. The next section of this paper details improvements in post-processing to preserve previously neglected radial and shear strain components to quantify the full 2D strain tensor for aortic cross-sections. Additionally, I will be introducing a semi-automatic approach to segmenting the aortic wall to improve repeatability and significantly shorten the time required for manual segmentation and analysis. Lastly, I will discuss the use of DENSE alongside MR flow analysis techniques to better quantify and correlate the full mechanical environment in the aortic arch to study how aortic fluid and tissue mechanics in individuals at elevated risk for aortopathies may differ from healthy volunteers.

2 Quantification of Radial and Shear Strain

This section has been adapted from work previously published in the Journal of Biomechanical Engineering (Copyright 2021 by ASME, adapted with permission). My contributions to this publication include data collection and analysis, drafting of the manuscript, revisions of the manuscript, and final approval of the version of the manuscript to be published. I would like to thank Dr. John Wilson for his role in conception and design of this study, drafting of the manuscript, revisions of the manuscript, and final approval of the version of the manuscript to be published. Please refer to the original article at:

P.A. Jones and J.S. Wilson, "The Potential for Quantifying Regional Distributions of Radial and Shear Strain in the Thoracic and Abdominal Aortic Wall Using Spiral Cine DENSE MRI," *J Biomech Eng*, vol. 143, no. 6, 2021.

2.1 Introduction

Mechanical homeostasis of the aorta is necessary for its proper function but can be disrupted due to aging, chronic conditions such as hypertension and atherosclerosis, and/or acute pathologies like aortic aneurysms and dissections [46]. In general, most pathological remodeling tends to stiffen the aortic wall; however, this stiffening can also be associated with notable regional heterogeneities, including susceptibility to highly focal areas of rupture risk. Thus, a reliable *in vivo* method for the regional quantification of patient-specific mechanical function in patients with aortopathy, and those at risk of their development, could significantly improve the early diagnosis, risk-assessment, and treatment planning for these pathologies that carry well-known risks for cardiovascular events.

Previous attempts to quantify aortic wall mechanics *in vivo* have included ultrasound, computed tomography (CT), and magnetic resonance imaging (MRI). Multiple studies have explored the ability of ultrasound to resolve the spatial distribution of aortic wall strain; however, these studies generally report only a homogeneous mean or peak strain and an overall spatial heterogeneity index rather than local strain values around the aortic circumference [47, 48]. Additionally, ultrasound faces difficulty resolving strains in the direction perpendicular to the direction of ultrasound propagation, such as in the lateral aortic walls, though recent exploration of multiperspective ultrasound imaging may improve this deficit [49]. Finally, although less expensive, ultrasound has less resolution and versatility for evaluating surrounding tissues compared to MRI and can have limited ultrasonographic windows for assessing deep structures.

Standard cine CT or MRI provide more resolved evaluations of deep peri-aortic tissues but have largely focused on providing homogenous values of wall strain based on geometric changes during the cardiac cycle (e.g., changes in cross-sectional area [50]). More advanced MRI techniques, such as strain-encoded (SENC) MRI [33] and phase-contrast tissue velocity mapping [35, 36], have attempted to quantify regionally heterogeneous cardiovascular mechanics *in vivo*; however, neither technique has produced clinically reliable quantitative maps of regionally heterogeneous strain around the aortic wall *in vivo*. Notably, since SENC calculates strain in the through-plane direction, estimating circumferential strain would require a longitudinal cross-section of the aorta, which is not only more difficult to align (particularly in the arch), but would likely suffer from increased partial volume effects due to high curvature of the aortic wall in the through-plane direction in this orientation. SENC can also be impacted by rigid body rotation along the imaging plane [29]. Phase-contrast tissue velocity mapping MRI can reveal regional displacements of the myocardium and was briefly explored for quantifying in vivo aortic wall

strain [51, 37], but this technique faces challenges in optimizing encoding gradients and the potential for accumulation of error through pixel-wise integration of velocity measurements over the cardiac cycle, especially in the presence of through-plane motion [29].

To overcome some of these challenges, 2D Displacement Encoding with Stimulated Echoes (DENSE) MRI has recently been explored as an alternative non-invasive method to quantify the heterogeneous distributions of circumferential strain of the aortic wall *in vivo* [20, 45]. Notably, 2D DENSE MRI can delineate local displacement with sub-voxel resolution and has been primarily developed to quantify regionally heterogeneous cardiac kinematics by assessing in-plane strains (e.g., circumferential, radial, and radial-circumferential shear in a short-axis slice) [40]. Unlike phase-contrast velocity mapping, DENSE directly encodes displacement data into the phase of each voxel. The results from the initial aortic DENSE studies suggested similar patterns of normalized circumferential strain around the aortic wall in discrete aortic regions in healthy volunteers when grouping by axial location (infrarenal, descending thoracic, or aortic arch), patient age, or average in-plane displacement angle of the aorta during local systole. In theory, these healthy distributions could potentially serve as a benchmark for identifying abnormal circumferential strain patterns in pathological aortas [45].

However, the previous studies made use of a post-processing method that spatially smoothed the displacement field of all pixels in the aortic wall without consideration of their radial location in the wall. This smoothing method reduces noise but eliminates potential differences in displacement between the luminal and adventitial layers of the wall, resulting in near-zero radial and shear strain values. Recovering and quantifying the full set of 2D strains including circumferential, radial, and shear may offer additional useful information for future clinical assessments of aortic pathology if such data can be reliably quantified in the thin aortic wall.

Therefore, this study aims to evaluate the feasibility and repeatability of assessing all components of the 2D aortic wall strain tensor by separately processing DENSE-derived kinematic data from the inner and outer layers of the aortic wall to preserve radial and shear data.

2.2 Methods

Imaging: For this study, all imaging data from Wilson et al. (2019) [45] was re-analyzed following a key modification to the post-processing algorithms as described below. In brief, 2D spiral cine DENSE images were obtained normal to the longitudinal axis of the aorta in healthy volunteers with no history of structural aortopathy at the infrarenal abdominal aorta (IAA, n=10), mid-descending thoracic aorta (DTA, n=13), and distal aortic arch (DAA, n=9). These axial locations were originally chosen based on clinical relevance to the location of common aortopathies including Type B aortic arch dissections (DAA), thoracic aortic aneurysms and dissections (DTA), and abdominal aortic aneurysms (IAA) [52]. All images were acquired on a 3T Siemens Trio or Prisma scanner using cardiac and respiratory gating, spiral k-space sampling, and fat suppression. Key parameters include 1.3 x 1.3 x 8 mm voxel dimension, TR 16 ms, TE 1.21 ms, flip angle 15°, in-plane displacement encoding frequency ω=0.17-0.25 cyc/mm, 18 spiral interleaves, 2 leaves per heartbeat, and 4 signal averages [45]. Scan time was approximately 8-10 minutes per axial slice without the use of acceleration or reduced phase field-of-view, depending on navigator efficiency. At each location, 18 timepoints were acquired through approximately the first two-thirds of the cardiac cycle to capture motion through local systole. Immediate repeat scanning was performed on six of the volunteers (two per location) to assess interscan repeatability. Note the original acquisition of the images was approved by the Emory University Institutional Review Board (IRB) and conducted following informed consent. All data was de-

identified before being approved by the Virginia Commonwealth University IRB for sharing and re-analysis.

Post-processing and Calculation of Strain: All post-processing was performed in MATLAB (Mathworks, Natick, MA) and utilized the aortic segmentations already performed in Wilson et al. (2019) [45]. In brief, DENSE phase images were unwrapped and used along with the magnitude images to manually segment the luminal aortic boundary at each time point. The adventitial boundary was segmented to ensure a wall thickness of at least two voxels (the minimum necessary to calculate 2D Green strain). Using the pixelwise DENSE phase data which proportionally encodes displacement, tracked position vectors were generated for each pixel within the aortic wall from the reference configuration at the end of cardiac diastole through local systole, as previously described [41].

Similar to Wilson et al. (2019) [45], multiple noise-reduction techniques were applied in post-processing, including time smoothing, reference point averaging, and displacement vector smoothing. However, unique to this study, an updated technique was applied for spatial smoothing of the displacement vectors to preserve radial and shear strain. The prior method spatially smoothed displacement vectors from all neighboring pixels in the aortic wall that were within a fixed number of pixel spaces surrounding the point of interest without discrimination to the radial location of the neighboring pixel. As a result, differences between inner and outer wall pixels were minimized, effectively eliminating any radial or shear strain. Herein, the innermost pixels of the aortic wall mask that line the lumen were processed separately from the remaining outer wall pixels to preserve potential radial gradients in displacement. Thus, the pixelwise spatial smoothing of displacement vectors occurred only with circumferential neighbors (as opposed to circumferential and radial neighbors as before) (Figure 2.1).

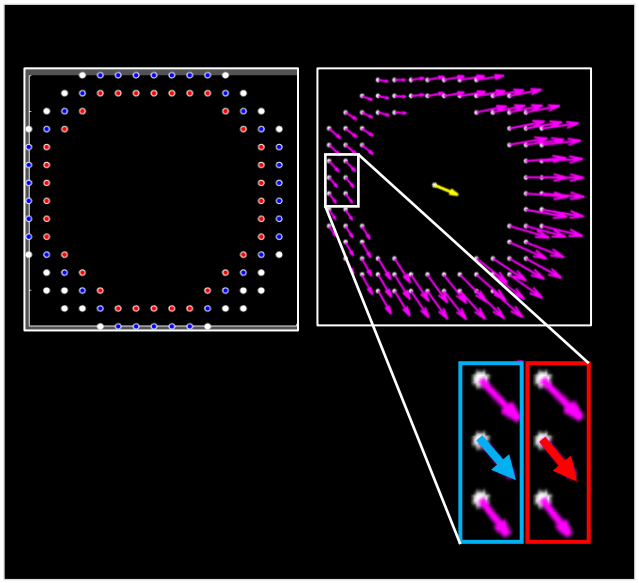

Figure 2.1: (Upper Left) Separation of inner wall (red) and outer wall (blue and white) pixels of the aortic wall mask. (Upper Right) DENSE-derived displacement vectors. (Lower Right) Schematic of independent spatial averaging of the displacement vectors for the inner and outer layers.

As before, the aortic wall was divided into 8 equally spaced sectors around its circumference, and the 2D Green strain ($\boldsymbol{E}$) was calculated from the referential displacement gradient ($\boldsymbol{H}$) for each sector using a quadrilateral finite element method as described by Humphrey [53], where

$$\boldsymbol{E} = \frac{1}{2}(\boldsymbol{H} + \boldsymbol{H}^T + \boldsymbol{H}^T \cdot \boldsymbol{H}), \text{ and } \boldsymbol{H} = \frac{\partial \boldsymbol{u}}{\partial \boldsymbol{X}}. \tag{2.1}$$

A standard transformation of the strain from *xy*-coordinates to local radial-circumferential coordinates was then performed. Next, a separate 8-sector strain map was generated using a half-sector rotation relative to the first map, and the resulting overlapping maps were combined using a 1:2:1 weighted spatial averaging to generate a final strain map with 16 unique equally spaced sectors. The interested reader is directed to Wilson et al., (2019) for full details [45].

To allow comparisons of strain distribution between volunteers with different mean values of strain, normalized circumferential strain (NCS), normalized radial strain (NRS), and normalized shear strain (NSS) at local aortic systole were calculated for each of the 16 sectors around the aortic wall as the regional strain value divided by the mean of the absolute value of each strain type for the given cross-section. As in the prior study, local aortic systole was defined as the time of greatest mean circumferential strain across all sectors for the IAA and DTA or the mean timepoint of the peaks of the six greatest circumferential strain sector values for the DAA.

Comparison of Post-processing Methods: The differences in regional distribution of circumferential strain using the original post-processing method (Method 1) and the new post-processing method that separately smooths the inner and outer aortic wall layers (Method 2) were assessed using the same imaging segmentations for the full set of volunteers at each axial location that were completed by one experienced reader for the earlier study by Wilson et al. (2019) [45].

Repeatability: Repeatability for post-processing Method 2 was assessed using the data from the six volunteers with repeated scans. Again, all manual imaging segmentations were those already completed for the earlier study by Wilson et al. (2019) [45]. Herein, only the updated post-processing technique was changed to allow for separate analysis of the inner and outer layers of the previously segmented aortic wall. In brief, ideal interscan repeatability was assessed for each component of strain between the two scans by a single non-blinded experienced 'Observer A' using calculations of the mean difference in strain (±SD), mean absolute difference in strain, mean normalized difference in strain (±SD), mean absolute normalized difference in strain, and the coefficient of variation. Similar quantitative comparisons were made for interobserver repeatably, where a second novice 'Observer B' was trained by Observer A using one set of the repeated scans and then independently analyzing the second set. Finally, intraobserver repeatability was assessed

by Observer A re-analyzing the data for the six patients more than a month following the original analysis.

Statistics: The mean absolute sector-by-sector difference (±SD) and coefficient of variation (CoV) of the difference between analysis with Method 1 versus Method 2 were determined for each volunteer at each axial aortic location for the circumferential, radial, and shear strains. Comparisons of mean strain between the two methods for each strain type and comparisons between the three strain types of the mean absolute difference and CoV of the difference in strains from the two methods were quantified by one-way ANOVA with a Tukey post hoc test. To evaluate each of the three types of repeatability tests (interobserver, intraobserver, and interscan), coefficient of variation (CoV) of the difference, sector-by-sector mean difference (±SD), and mean absolute difference (±SD) were calculated for each type of strain for both the standard strain data and normalized strain data. Comparisons of mean differences between strain types for each repeatability test were also performed by one-way ANOVA with a Tukey post hoc test. Statistical analyses were performed in SPSS (IBM SPSS Statistics, Version 26.0. Armonk, NY), and significance was defined as $p<0.05$.

2.3 Results

Comparison of post-processing methods: The new post-processing technique resulted in mean absolute differences in circumferential strain of <2% at all axial locations (Figure 2.2, Table 2.1) and failed to show a difference in mean circumferential strain ($p=0.997$). In contrast, mean absolute values of radial and shear strain were significantly greater in Method 2 compared to Method 1 (Table 2.1; $p<0.001$ and $p<0.05$, respectively). Similarly, mean absolute differences of radial (0.043±0.05) and shear strain (0.044±0.04) between methods were greater than those for

circumferential strain (0.013±0.01) ($p<0.001$ for both). Comparing mean coefficients of variation (CoV) of the differences between the methods, where each CoV value was calculated as the standard deviation of the difference in strain divided by the mean strain of the two methods, also revealed that relative differences in circumferential strain were significantly smaller than radial and shear strain (Table 2.1, $p<0.001$ for both) and that relative differences in shear strain were significantly smaller than radial strain ($p<0.001$).

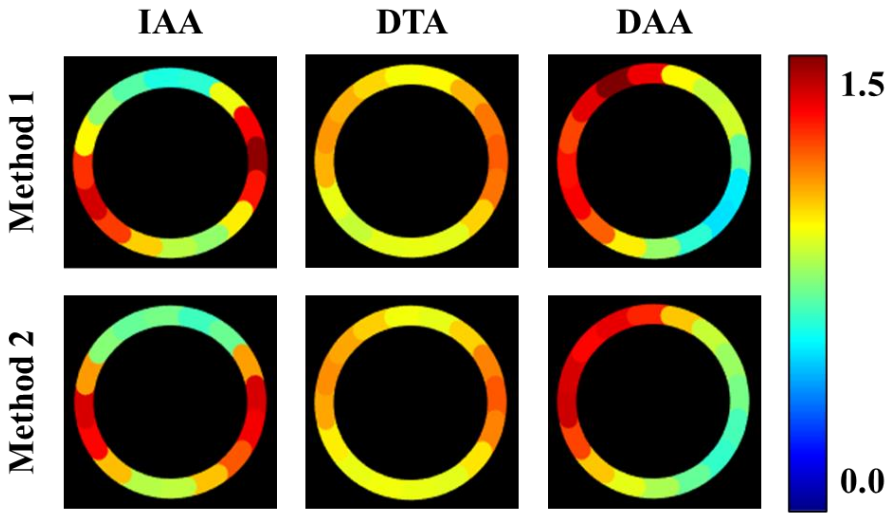

Figure 2.2: Mean values of normalized circumferential strain across all volunteers for each axial location along the aorta between Method 1 & Method 2.

Table 2.1: Mean absolute differences and coefficient of variation (CoV) of differences in circumferential strain (Ecc), radial strain (Err), and shear strain (Erc) between Method 1 & Method 2.

		IAA	DTA	DAA	Average
E_{cc}	**Mean Abs. Diff. (±SD)**	0.017 ± 0.02	0.015 ± 0.01	0.008 ± 0.01	**0.013 ± 0.01**
	CoV (Mean Diff.)	0.256 ± 0.16	0.092 ± 0.04	0.189 ± 0.26	**0.179 ± 0.15**
E_{rr}	**Mean Abs. Diff. (±SD)**	0.054 ± 0.06	0.042 ± 0.04	0.034 ± 0.04	**0.043 ± 0.05**
	CoV (Mean Diff.)	1.600 ± 0.28	1.382 ± 0.43	1.224 ± 0.60	**1.402 ± 0.44**
E_{rc}	**Mean Abs. Diff. (±SD)**	0.041 ± 0.04	0.045 ± 0.05	0.047 ± 0.03	**0.044 ± 0.04**
	CoV (Mean Diff.)	1.400 ± 0.32	0.449 ± 0.20	0.782 ± 0.38	**0.877 ± 0.30**

Repeatability measures: Table 2.2 records the mean coefficient of variation (CoV) of the differences in circumferential strain for each type of repeatability (interobserver, intraobserver, and interscan) at each axial location and the average for all three locations. No significant difference in average CoV was found between any of the repeatability tests when comparing post-processing Method 1 and Method 2 for this small study. For each repeatability test and for both methods, the DAA demonstrated the largest CoV for repeatably quantifying circumferential strain, which may be due to the larger and more complex displacements in this aortic region with significant curvature. In all but one case, the IAA demonstrated the smallest CoV.

Table 2.2: Mean coefficient of variation (CoV) of differences in circumferential strain between each type of repeated scan using either Method 1 (CoV-1) or Method 2 (CoV-2).

		IAA	DTA	DAA	Average
Interobserver Repeatability	**CoV - 1**	0.112	0.215	0.383	**0.237 ± 0.11**
	CoV - 2	0.172	0.237	0.450	**0.286 ± 0.12**
Intraobserver Repeatability	**CoV - 1**	0.105	0.220	0.324	**0.216 ± 0.09**
	CoV - 2	0.194	0.250	0.348	**0.264 ± 0.06**
Interscan Repeatability	**CoV - 1**	0.181	0.217	0.328	**0.242 ± 0.06**
	CoV - 2	0.210	0.144	0.301	**0.219 ± 0.06**

Since radial and shear strains can take both positive and negative values, mean values of these components of strain can approach zero, making CoV an unreliable metric. Thus, mean difference (±SD), mean absolute difference, mean normalized difference (±SD), and mean absolute normalized difference were calculated for each type of repeatability study and strain component for Method 2 (Table 2.3), noting that normalization was performed using the patient-specific mean of the absolute values of each strain component across all 16 sectors. For all repeatability tests, circumferential strain demonstrated the lowest mean absolute difference (range 0.02-0.03), and radial strain demonstrated the highest mean absolute difference (range 0.05-0.06). Shear strain had moderate mean absolute differences (range 0.03-0.05). However, when comparing the three components of strain for each repeatability test, only the radial strain for the intraobserver comparison achieved statistical significance for having a greater mean absolute difference ($p<0.03$ compared to circumferential strain; $p<0.05$ compared to shear strain). For all three repeatability tests, the mean absolute normalized difference in circumferential strain was significantly less than that for radial strain ($p<0.05$). For interobserver and interscan repeatability, mean absolute normalized difference in circumferential strain was also significantly less than that for shear strain ($p<0.005$). No clear correlation to axial aortic location was identified for the reproducibility of normalized radial and shear strains.

Table 2.3: Mean difference (±SD), mean absolute difference, mean normalized difference (±SD), and mean absolute difference in normalized circumferential (Ecc), radial (Err), and shear (Erc) strains for interobserver, intraobserver, and interscan repeatability tests using Method 2.

	Strain	Mean Diff. ± SD	Mean Abs. Diff.	Mean. Diff. ± SD (Norm)	Mean Abs. Diff. (Norm)
INTEROBSERVER	**Ecc**	-0.009 ± 0.03	0.033	0.000 ± 0.28	0.228
	Err	-0.029 ± 0.06	0.059	-0.274 ± 0.72	0.691
	Erc	0.006 ± 0.05	0.045	0.053 ± 0.74	0.694

	Strain	Mean Diff. ± SD	Mean Abs. Diff.	Mean. Diff. ± SD (Norm)	Mean Abs. Diff. (Norm)
INTRAOBSERVER	**Ecc**	0.001 ± 0.03	0.025	0.000 ± 0.26	0.210
	Err	-0.017 ± 0.05	0.045	-0.267 ± 0.70	0.665
	Erc	0.013 ± 0.03	0.026	-0.214 ± 0.62	0.566

	Strain	Mean Diff. ± SD	Mean Abs. Diff.	Mean. Diff. ± SD (Norm)	Mean Abs. Diff. (Norm)
INTERSCAN	**Ecc**	-0.001 ± 0.03	0.023	0.000 ± 0.20	0.182
	Err	-0.002 ± 0.07	0.060	0.004 ± 1.04	0.975
	Erc	0.005 ± 0.05	0.049	0.294 ± 0.84	0.878

Spatial distribution of normalized strain by group: Mean distributions of normalized circumferential strain (NCS), normalized radial strain (NRS), and normalized shear strain (NSS) calculated by Method 2 were mapped for each axial location, as well as between previously suggested subgroups at each location as identified by Wilson et al. (2019) based on trends in distributions in circumferential strain (Figure 2.3) [14]. These include division of the DTA cohort into volunteers with a positive mean displacement angle (i.e., toward the left anterolateral chest wall) and those with a negative mean displacement angle (i.e., toward the left posterolateral chest wall), and division of the DAA cohort into volunteers ≥50 years of age and those under 50 years of age.

The spatial distribution of NCS using Method 2 was similar to the results using Method 1 for all locations and groups. For example, the largest NCS remained in the lateral walls in the IAA

(1.37 ± 0.4 in the left lateral wall, 1.37 ± 0.3 in the right lateral wall), in the medial wall in the DTAs with a positive mean displacement angle (1.23 ± 0.2), and in the left lateral wall in DTAs with a negative displacement angle (1.30 ± 0.3) (Figure 3). Similarly, as in the previous study using Method 1, DAA volunteers <50 years of age demonstrated maximum NCS at peak systole along the greater curvature (1.93 ± 0.2)**,** while volunteers ≥50 years demonstrated peaks along the inferomedial wall nearer to the lesser curvature (2.05 ± 0.6)**.**

Mean distributions of NRS and NSS using Method 2 are shown in Figure 2.3 for each location, including the suggested age-based subgroups for DAA from the previous analysis. The DTA subgroups based on displacement angle did not reveal distinct differences in mean NRS or NSS and thus were grouped together. The corresponding peak magnitude values can be seen in Table 2.4.

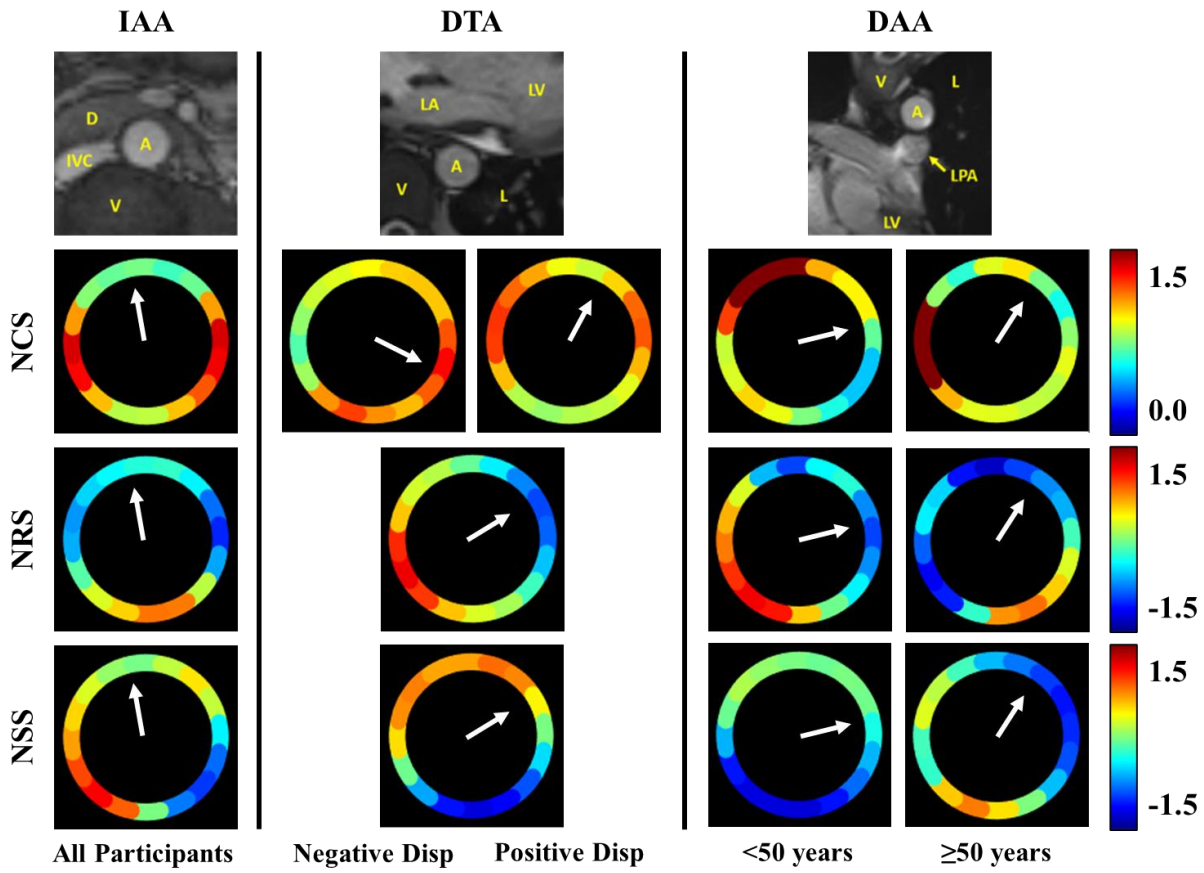

Figure 2.3: Mean distributions of NCS, NRS, and NSS for each of the three axial locations, with DTA split into subgroups by displacement angle for NCS and DAA split into subgroups by age for all strain types. Arrows represent the mean displacement direction of the aorta at local systole at each location. (A – aorta, V – vertebra, L – lung, LA – left atrium, LV – left ventricle, LPA – left pulmonary artery, D – duodenum, IVC – inferior vena cava)

Table 2.4: Maximum and minimum values and corresponding in-plane location for NCS, NRS, and NSS for each of three axial locations and subgroups as shown in Figure 3.

		NCS		NRS		NSS	
		Magnitude (Max)	**Location**	**Magnitude (Max/Min)**	**Location**	**Magnitude (Max/Min)**	**Location**
IAA		1.37 ± 0.4, 1.37 ± 0.3	Left Lateral, Right Lateral	0.78 ± 1.4, -1.03 ± 0.8	Posterior, Left Lateral	1.13 ± 0.5, -0.97 ± 1.3	Right Posterolateral, Left Posterolateral
DTA	**Neg. Disp.**	1.30 ± 0.3	Left Lateral	1.17 ± 0.8, -0.91 ± 1.1	Posteromedial, Anterolateral	0.80 ± 1.0, -1.24 ± 0.5	Anterior, Posterior
	Pos. Disp.	1.23 ± 0.2	Medial				
DAA	**< 50 years**	1.93 ± 0.2	Greater curvature	1.15 ± 0.9, -0.71 ± 1.2	Inferomedial, Greater curvature	0.14 ± 0.8, -1.25 ± 1.3	Greater Curvature, Lesser Curvature
	≥ 50 years	2.05 ± 0.6	Medial	0.79 ± 0.9, -1.3 ± 1.0	Left Inferolateral, Greater curvature	0.76 ± 1.0, -1.09 ± 1.1	Lesser Curvature, Left lateral

2.4 Discussion

Patient-specific mechanical analysis of the aorta would be improved by the ability to reliably quantify all components of the 2D Green strain tensor around the aortic wall *in vivo* using DENSE MRI. In contrast to the previous processing method that effectively eliminated radial and shear strain due to spatial smoothing of the displacement data throughout the aortic wall, the updated post-processing method presented herein recovered non-zero regional values of radial and shear strain (mean absolute increase of 4% strain for both) while preserving the regional circumferential strain measurements from the original post-processing method (mean absolute difference of only 1% strain) (Figure 2.2, Table 2.1). Relative repeatability of the circumferential strain measurements was also preserved (Table 2.2). These results open the possibility for future

exploration of the diagnostic usefulness of the newly quantifiable *in vivo* regional radial and shear strain distributions.

Across the interobserver, intraobserver, and interscan repeatability tests for the new post-processing method, the circumferential strain demonstrated the best reproducibility, followed by the shear strain and then radial strain, particularly when comparing normalized data (Table 2.3). The overall mean absolute difference in normalized circumferential strain for all three repeatability tests was only 21% (i.e., the average sector-to-sector difference in a repeated scan is 21% of the patient-specific mean strain); however, the same metric for normalized shear and radial strains was 71% and 78%, respectively. The difference in repeatability in terms of strain type is not unexpected and is likely due to the thinness of the aortic wall relative to its circumference, as there are more pixels around the aortic wall (on average 4-5 per measured sector) from which to derive circumferential strain than pixels in the radial direction through the aortic wall (on average only 2) from which to derive radial strain and radial-circumferential shear strain. Thus, user-variability in manually segmenting the aortic wall and partial volume effects contribute significantly more variability to the radial and shear calculations. This result suggests that any future use of patient-specific measures of NRS or NSS to diagnose regional mechanical pathology will have to represent a larger deviation from the healthy radial and shear strain distributions than could be discerned for local changes in circumferential strain.

When applying the updated post-processing method to the entire data set, the previously described location-specific patterns of normalized circumferential strain (NCS) distribution were again evident (Figure 2.3), demonstrating that assessments of radial and shear strain distribution can be performed without sacrificing the quantification of regional circumferential strain. Like the NCS, the normalized radial strain (NRS) and normalized shear strain (NSS) were heterogeneously

distributed around the circumference of the aortic wall and depended on the axial location; however, when comparing across the subgroups previously identified by NCS distribution, only the DAA subgroups based on age demonstrated clear differences in NRS and NSS. Nevertheless, some interesting observations can be made regarding the overall mean NRS and NSS at the IAA and DTA as well.

For the infrarenal abdominal aorta and descending thoracic aorta, the greatest mean NRS was located adjacent to the aorto-vertebral interface (AVI) (i.e., in the posterior wall of the IAA and the posteromedial wall of the DTA; Figure 3). Notably, this is the same area where the aorta may be tethered to the vertebral column via periadventitial connective tissue (c.f., [54, 55]). Indeed, aortic DENSE reveals generally decreased displacement and circumferential strain at the AVI in the IAA and DTA, consistent with the few previous studies using speckle-tracking ultrasound or phase-contrast tissue velocity mapping MRI that reported low regional displacement or strain near the spine [48, 37, 56]. For the IAA, the average peak displacement vector at local systole was 96^{o} relative to a horizontal axis pointing along the positive x-axis in the image (generally, the patient's left side). For the DTA, the average peak displacement was 40^{o}. Thus, the mean displacement of the IAA is anterior (consistent with previously published ultrasound results [57]), and the mean displacement of the DTA is anterolateral – both directly away from their potential tether points near the vertebra with elevated NRS.

Two possibilities exist to explain this elevated radial strain. First, the bulk motion of the aorta away from the vertebra places the connection between the aortic adventitia and vertebra into tension, creating a positive radial strain in the aortic wall (which would otherwise be expected to be negative due to the increased internal pressure during local systole). Second, the thinness of the aortic wall and resulting partial volume effects of the two-pixel thick aortic mask results in the

outer pixel including signal from the stationary connective tissue around the vertebra. Thus, as the aorta moves away from the vertebra, the distance between the stationary vertebra and aortic wall slightly increases, resulting in a false perception of increased radial strain. It is possible that both effects may contribute to the increased NRS. This is a challenging question that will require future tests to determine; nevertheless, the correlation of increased NRS with known anatomic features and physiologic boundary conditions suggest that the elevated NRS in the wall near the vertebra is not simply noise, but rather may be able to provide useful information about aortic boundary conditions and, if not due solely to partial volume effects, periaortic tethering. In further support of the logical consistency of the radial strain distribution, the most negative mean radial strains were located in the lateral walls of the IAA and left lateral wall of the DTA, consistent with an expected thinning of the wall at these locations with elevated NCS (Figure 2.3).

Similarly, the distribution of mean shear strain in the IAA and DTA can be explained by the bulk motion of the aorta relative to the expected tethering at the vertebra. Note that mean NSS has greatest magnitude, but opposite sign, on either side of the aorto-vertebral interface for both locations (posterolateral walls for IAA and anterior and posterior walls for DTA), straddling the area of high NRS at the tether point. As the aorta moves in the direction of its mean displacement angle but is constrained along its adventitia adjacent to the vertebra, it is possible that the inner layer of the aorta slides slightly anteriorly relative to the focally constrained adventitial layer. This would result in a clockwise (positive) shear of the inner layer on the outer layer in the sectors immediately clockwise to the tether point and a counterclockwise (negative) shear in the sectors immediately counterclockwise to the tether point – exactly as seen in Figure 3. Notably, this elevated magnitude of shear strain is remarkably consistent with the recent computational results of Petterson et al. (2019) [56], which predicted elevated radial-circumferential shear strain along

the posterolateral aortic walls when including a simulated stiff vertebra posterior to the aorta. In addition, since the mean aortic wall motion is directed away from the vertebra, the opposite wall would be moving purely radially and thus should have minimal shear – also as shown for both the IAA and DTA in Figure 3. Again, these relative shear strains could also be affected by partial volume effects of the aortic wall sliding against stationary peri-aortic tissues surrounding the aortic walls. Thus, we interpret these results cautiously and encourage future investigations.

In contrast to the IAA and DTA, the aortic arch is susceptible to greater flow asymmetry due to its curvature and large asymmetric branch points (note the images were acquired within a few centimeters distal to the left subclavian artery). The tethering and peri-aortic tissues at this location are also more complex. As the DAA curves posteriorly and inferiorly, it approaches the vertebral column, but does not have direct proximity as in the IAA and DTA; thus, the exact tethering is unclear. The inferior wall of the DAA also abuts the left pulmonary artery (LPA) at this location, which as a pressurized vessel has its own motion. In addition, the ligamentum arteriosum connects the aorta to the LPA near this location in the majority of patients. Finally, the proximity of the DAA to the heart may impart greater longitudinal and twisting motions at this location compared to the DTA and IAA.

Using the new method for post-processing of the DAA data reproduces the previously identified differences in mean NCS distribution for volunteers <50 years of age and those ≥50 years (Figure 3). Interestingly, mean NRS and NSS also demonstrate differences in these two subgroups. In the younger group, the greatest mean NRS is located along the inferomedial wall between the aorto-vertebral interface and the likely connection of the ligamentum arteriosum to the LPA. As with the IAA and DTA, the average peak displacement vector for this subgroup (19^{o}) points away from this region and towards an area of relatively low NRS. Additionally, the region

of greatest mean NCS along the greater curvature is associated with a lower mean NRS, as expected. As with the IAA and DTA, the NSS is split with more positive values in the sectors clockwise to the region of high positive NRS and more negative values counterclockwise to this region. However, the NSS values along the greater curvature are closer to zero rather than highly positive, and those along the lesser curvature are highly negative and may be influenced by the motion of the underlying LPA.

For the volunteers ≥50 years of age, the distribution of NRS appears as a mirror image to the younger group, with the greatest NRS now shifted to the left inferolateral wall. Notably, the average peak displacement angle for this subgroup (45^{o}) is no longer directed opposite of the region of greatest NRS as in all the other groups, suggesting a potentially unique dynamic in this subgroup. However, the greatest and least mean NSS still straddle the region of high NRS. This results in the inferior wall of the aorta in the older group demonstrating a positive peak in the exact same location that the younger group demonstrated a negative peak (i.e., the shear strain reversed directions). The exact cause of these differences in DAA strain between the older and younger volunteers requires more testing; however, one potential explanation that accounts for all kinematic observations is that the inferior wall of older DAAs may be acted upon by an inferiorly oriented periadventitial force. This would increase the relative NCS along the inferomedial wall as the force strains the segment of wall between its application point and the normal tethering point, induces a positive NRS along the inferolateral wall, and reverses the NSS as the adventitial surface is pulled away from the overall direction of the aortic motion.

Physiologically, this downward force could be explained by changes in the relative motion of the LPA relative to the DAA transmitted through the ligamentum arteriosum to the adventitia of the aorta. Since aortic stiffness is known to increase with age on average, this increased stiffness

and faster transmission of the luminal pressure wave may affect both the magnitude and timing of local systole at the DAA relative to completion of cardiac systole. That is, in older volunteers with stiffer aortas, the contracting heart is still pulling the aorta and pulmonary trunk inferiorly when the pressure wave reaches the DAA, and the reduced elasticity of the stiffened great vessels prevents any dampening of this inferior force as would be seen in younger healthier vessels. Thus, the heart, pulmonary trunk, LPA, and DAA (through the connection at the ligamentum arteriosum) may form a mechanically coupled unit independent of the deformation caused by the pulse pressure from the blood flow. Future studies are underway to explore this mechanical paradigm, but it is an intriguing hypothesis considering that this portion of the DAA is known to be at high risk of aortic dissection (Type B) [58] and that the connection of the ligamentum arteriosum has already been implicated in traumatic aortic dissections [59].

Limitations of this work include the small sample size (n=6 for the repeatability component of this study and n=32 for the axial location comparisons), the need for manual segmentation of the aortic wall which introduces user-specific error, and the non-blind nature of the idealized interscan repeatability test [45]. The primary technical limitation is the maximum imaging resolution that aortic DENSE MRI can obtain while ensuring adequate signal-to-noise for regional strain quantification, which constrains the aortic wall mask thickness to approximately 2 pixels in most cases. As noted above, the limitation in the number of pixels through the wall in the radial direction is likely a primary cause of the reduced repeatability of quantifying radial and shear strain compared to circumferential strain for the thin aortic wall. These limitations may be improved in future studies by developing auto-segmenting algorithms to reduce user error, continuing to optimize parameters and techniques on current 3T scanners, and potentially expanding the use of

DENSE MRI to 7T clinical imaging, though issues with field inhomogeneities and elevated specific absorption rates would need to be considered and overcome.

2.5 Conclusion

We conclude that the new post-processing technique that independently assesses the inner and outer aortic wall layers has potential for improving the patient-specific regional quantification of radial and shear strain from aortic DENSE data; however, further studies and technical advancements are required to improve its repeatability to the level of the circumferential strain data and to assess the influence of potential partial volume effects. Thus, pathological changes in radial and shear strain distribution would have to be large to distinguish them from healthy distributions of NRS and NSS. Nevertheless, the mean distributions of NRS and NSS in this structurally normal data set demonstrate logical spatial correlation to important peri-aortic tissues that are location-specific along the length of the aorta. Thus, this improved aortic DENSE MRI technique may provide a unique opportunity to investigate and quantify regional heterogeneities in aortic tethering, mechanical boundary conditions, and potential focal vulnerabilities in order to improve clinical diagnostics and patient-specific computational models of aortic biomechanics.

3 A Semi-Automatic Approach to Segmenting the Aortic Wall using DENSE MRI

3.1 Introduction

Future applications of DENSE MRI for evaluating vascular disease in the clinical setting are promising; however, they are currently limited by lengthy postprocessing times and limited repeatability. The most time-intensive step, and one of the primary sources of error contributing to lower repeatability with vascular DENSE imaging, is the reliance on manual segmentation to create the mask of the aortic wall required for analysis. Manual segmentation of an aortic wall mask requires marking the luminal and adventitial borders of the aorta for every cross-section image in the cine set, which can take over an hour for a trained observer to complete. The time-intensive process reduces the clinical utility of this approach for high throughput evaluation and serial monitoring of patients with aortopathies, such as aortic aneurysms and dissections. Automating the segmentation process would allow for faster turnaround and help to reduce the effect of observer bias for strain analysis of the aortic wall.

One basic approach to automating segmentation in medical images is to utilize signal intensity histograms, such as in the conventional Otsu method for single or multiple level thresholding [60]. The signal histograms in MRI can represent a variety of parameters including T1 or T2 relaxation constants, proton density, or phase values depending on the sequence used to acquire the images [61]. Thresholding methods including Otsu's method, fuzzy logic techniques, and clustering allow for easier implementation of edge detection approaches such as Sobel or Canny methods [62, 63]. These edge detection-based methods are reliable for imaging with high spatial resolution and good contrast, such as to delineate the endocardial border in late gadolinium

enhanced-MRI. Unfortunately, they are less reliable for low resolution imaging or in the presence of noise [64]. Alternative approaches to segmentation in low-contrast images include active contour models and graph cut methods, which depend on the minimization of boundary and curvature-based energy functions to overcome the limitations of edge detection methods by preventing open contours or regions [61]. However, these active methods are sensitive to initialization parameters. The reliance on global optimization to choose the strongest borders can also result in the 'detection' of false edges without additional temporal restrictions or shape priors [65, 66].

Another technique, classified as prior knowledge-based methods, take advantage of large image atlases or training sets to prime a method to prioritize specific features in segmentations, including curvatures, shapes, or image intensity [67, 68, 69]. The most widely used atlas-based segmentation methods involve non-rigid registration of an already segmented atlas (generally segmented manually) to an input image, where the transformed points along the atlas contours become the starting point for edge detection to refine boundaries in the input image [70]. These methods can be computationally expensive depending on the registration process used, and the accuracy of the result is dependent on the atlas quality, including the accuracy of manually defined contours and the closeness of approximation of the atlas to the anatomy of interest [61, 64].

More recently, many machine learning-based methods have been introduced (for example, for fully automatic segmentation of both the left ventricle and the thinner right ventricle wall [71, 72, 73, 74, 75]). Deep learning has also been used with DENSE MRI for both automatic segmentation and phase unwrapping in healthy controls and patients with cardiovascular complications [76, 77]. The use of machine learning to overcome many of the limitations of traditional automatic segmentation techniques, especially for smaller structures like the right

ventricular wall, shows potential promise for segmentation of the aorta. However, machine learning methods like convolutional neural networks require a large amount of data to train on, and the results are limited by how representative the training data set is, especially when working with poor quality scans or images with abnormal anatomy.

In aortic DENSE imaging, however, the signal intensity of the image is not the only characteristic available to automate segmentation. Similar to previous work on segmentation of the left ventricle using DENSE MRI [78], we aimed to develop a segmentation tool that employs the unique displacement data obtained from the DENSE sequence to guide contouring. The goal of this iterative semi-automatic segmentation algorithm was to both shorten the lengthy postprocessing time required for aortic DENSE scans while simultaneously reducing the user-dependent error introduced by manual segmentations.

3.2 Methods

2D aortic DENSE MRI data from Wilson et al. [45] acquired in the proximal descending aorta (PDA, n = 8), mid-descending thoracic aorta (DTA, n = 13), and infrarenal abdominal aorta (IAA, n = 10) were re-analyzed following the implementation of a novel semi-automatic masking algorithm in MATLAB (Mathworks, Natick, MA). DENSE magnitude images were used to manually demarcate a rough initial mask containing the aortic wall and 2-3 adjacent luminal and periaortic voxels on either side of the wall (Figure 3.1) for each time point. Initial analysis was run on all voxels within the mask at each time point to calculate displacements relative to the reference configuration (timepoint 1) from the voxel phase signal, as introduced in equation 1.8 in Chapter 1. The back-projected *xy*-coordinates ($\boldsymbol{X}$,$\boldsymbol{Y}$) at the reference configuration at time t=1 for all voxels

$(i = 1, 2, \dots, M_t)$ from every future timepoint $(t = 2, 3, \dots, N)$ were then calculated using equations 3.1 and 3.2 and overlaid on the reference configuration (Figure 3.2), where

$$\boldsymbol{X} = \cup_{t=2}^{N}\left(\cup_{i=1}^{M_t}\left(x_{i,t} - \Delta x_{i,t}\right)\right) \tag{3.1}$$

$$\boldsymbol{Y} = \cup_{t=2}^{N}\left(\cup_{i=1}^{M_t}\left(y_{i,t} - \Delta y_{i,t}\right)\right) \tag{3.2}$$

and x and y are the voxel positions at all timepoints after reference, and Δx and Δy are the DENSE-derived displacements.

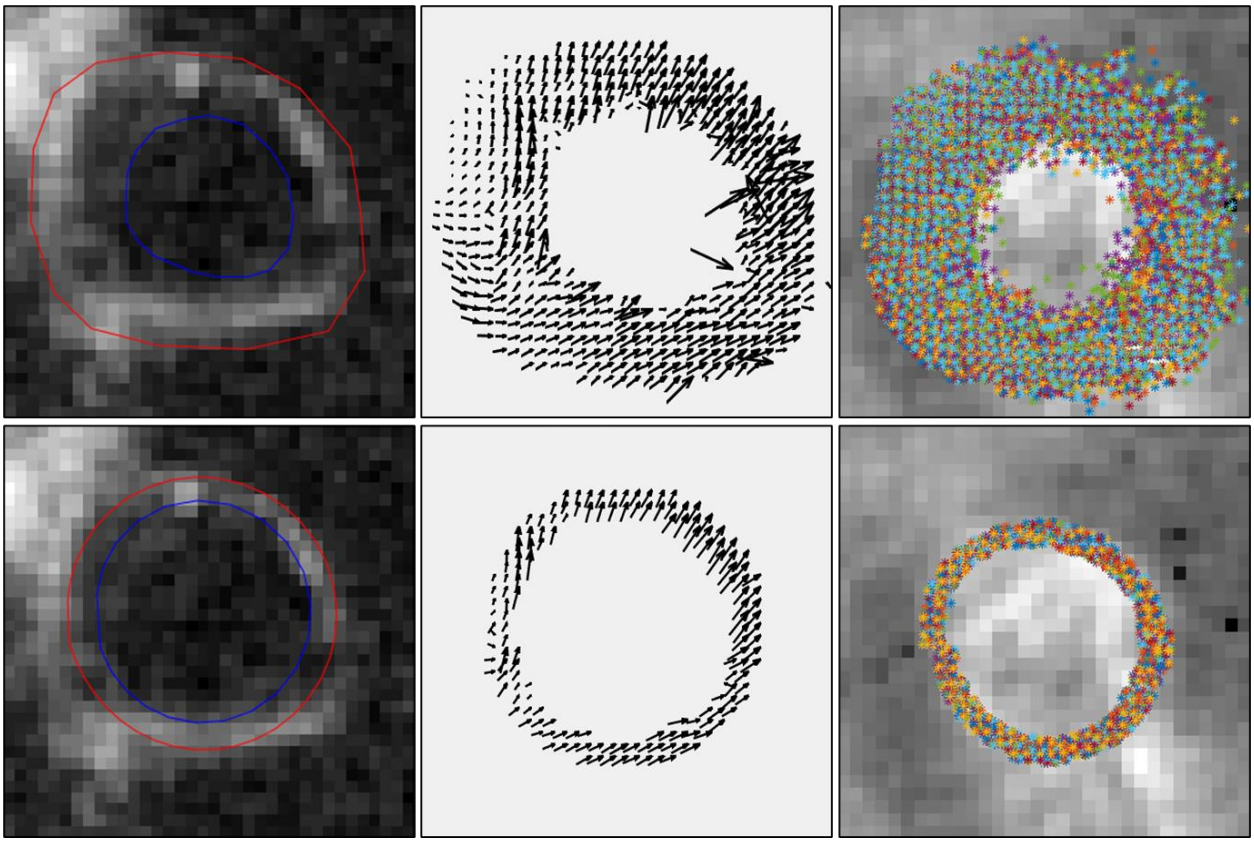

Figure 3.1: (*Top Row*) Example of initial rough masking in the descending aortic arch (*left*), with the displacement vectors for this mask from reference timepoint (*middle*) and back projections of all timepoints to reference (*right*). (*Bottom Row*) Final masking (*left*), final displacement vector field (*middle*), and back projections of all timepoints to reference (*right*).

In addition to the raw back-projected position data, the tracked position vectors (TPV) from the DENSE-derived displacements were used. TPV vectors represent the stepwise path of voxels included in the reference mask through subsequent timepoints, where displacements for a given TPV is calculated by interpolation of the three nearest raw displacement vectors. Path linearity for each TPV was determined by the ratio of the largest singular value to the second largest singular value as calculated by singular value decomposition (SVD), where a higher ratio is indicative of a more linear path. Spatial distribution of a tracked point over time was calculated as average pairwise distance between its position at each timepoint and the centroid of its total positions over time. The TPV were divided into 16 circumferential groups based on original position at reference time, and the intersection of the top 66% of points by path linearity and top 66% of points by average distance to centroid was obtained for each sector. These points were saved for weighting the initial reference mask.

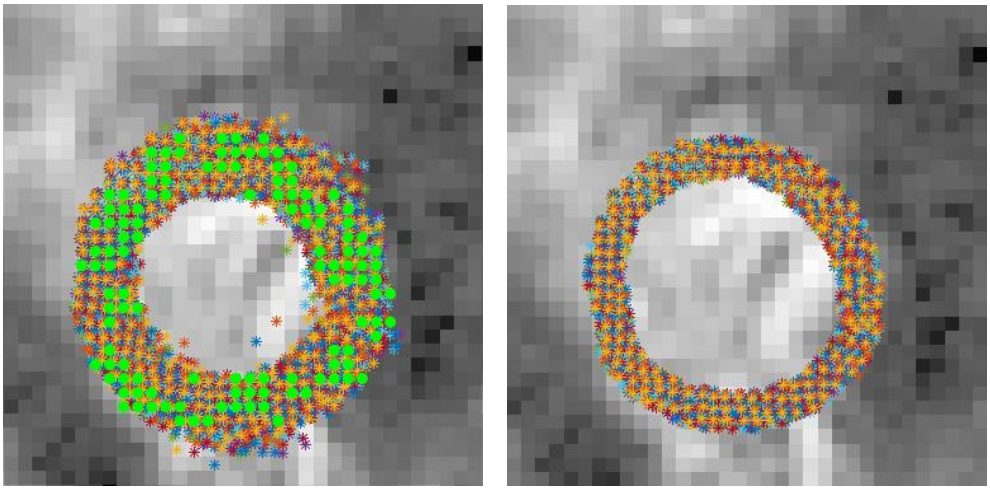

Figure 3.2: (*Left*) Back-projected points at reference time with the initial position of the saved TPV points shown as green circles. (*Right*) Result after all points outside one standard deviation of the centerline are eliminated. Different colors represent voxels displaced from different timepoints.

The cluster of back-projected data points at timepoint 1 was similarly divided into 16 equally sized circumferential sectors matching those of the TPV groups. For each sector, the weighted mean radius and standard deviation of radius were found by averaging the radii of the back-projected points along with the saved TPV *xy*-positions in timepoint 1 adjusted by a 10-fold weighting factor to represent the higher likelihood that the filtered TPV were located on the true aortic wall. The points located within one standard deviation of the mean radius for each sector (Figure 3.3) were saved and used to generate a 2D convex alpha shape bounding area (determined from the Delaunay Triangulation, as outlined in [79, 80]). The resulting alpha shape was used to define the updated mask of the aorta at the reference timepoint shown in Figure 3.4.

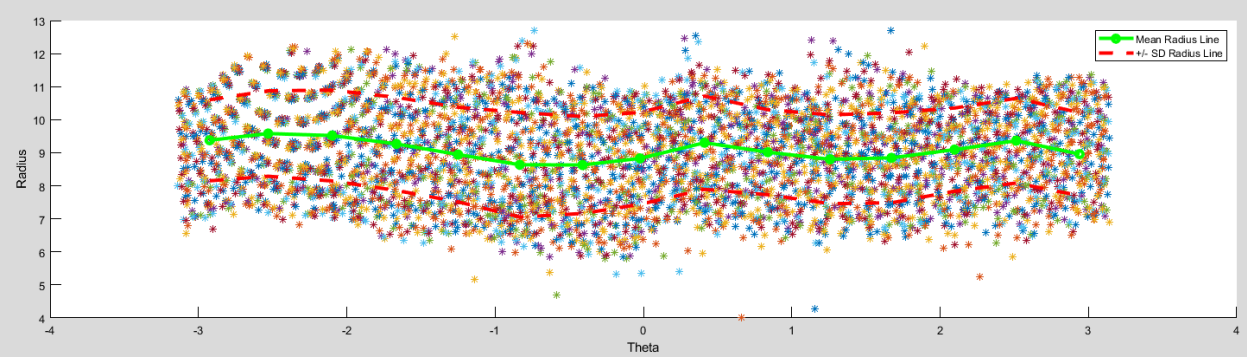

Figure 3.3: Back-projected points converted to a polar coordinate system and unwrapped from negative to positive π-radians. The weighted mean radius is shown as a green solid line, and the radii representing one standard deviation above and below the mean are shown as dashed red lines.

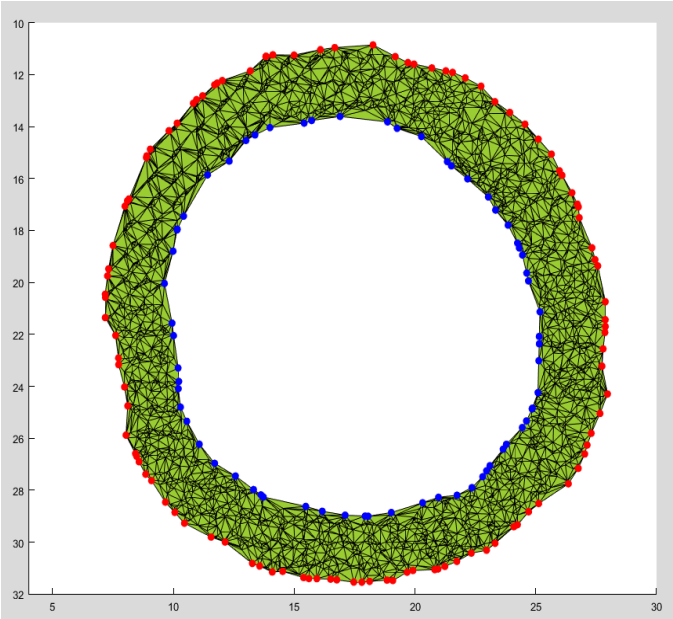

Figure 3.4: Result from 2D convex alpha shape of remaining points at reference time, with inner contour vertices shown as blue circles and outer contour vertices shown as red circles.

After establishing an updated mask for the reference timepoint, each mask at subsequent timepoints was updated by eliminating points that, when projected by their displacement data back to the reference timepoint fell outside of the updated reference mask. Four and eight-connectivity adjacency matrices were generated for the remaining points in each timepoint mask and used to build directed graph objects to determine the number of neighbors for each point and the cluster that each point belonged to. Points that did not meet the adequate neighbor criteria (defined as points with fewer than 3 neighbors in 8-connectivity, and fewer than 2 neighbors in 4-connectivity) or points that did not belong to the primary cluster were dropped. This was done to eliminate sharp outcroppings from the mask or points that were not connected to the primary cluster representing the aortic wall. The remaining points were used to generate a 2D bounding area as explained for the reference timepoint. The *xy*-coordinates were obtained from the inner and outer borders of the updated bounding areas, converted to polar coordinates, and spatially smoothed with a fifth-degree

polynomial to produce the inner and outer mask contours for a given timepoint. These steps were repeated for all timepoints after reference.

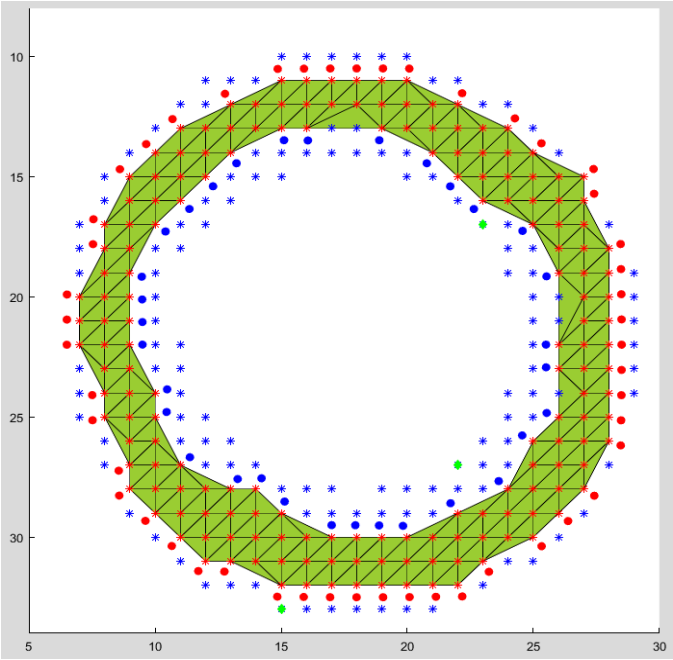

Figure 3.5: Example of mask for later timepoint, where the blue stars represent points that were excluded due to falling outside the acceptable range in the reference mask. Green circles show points that were eliminated by connectivity checks.

The full segmentation process from back-projection of points to reference through the generation of smoothed inner and outer wall contours for each timepoint was repeated iteratively until the mask generated at reference reached a thickness of two voxels (the minimum necessary to calculate 2D Green strain). The masks were then used for strain analysis, as detailed in Chapter 2 and previous reports [20, 45, 81].

Statistics: Strain results using the novel semi-automatic segmentation were compared to results from manually segmented masks from two or three observers depending on axial location (n = 3 for PDA and IAA, n = 2 for DTA). The mean absolute sector-by-sector difference (±SD)

and coefficient of variation (CoV) of the difference for normalized circumferential, radial, and shear strains obtained from manual and automatically generated masks were determined for each volunteer at each axial location. The differences in mean absolute difference and CoV of difference by axial location and strain type were assessed using Kruskal-Wallis one-way analysis of variance with Dunn post hoc test. Associations between mean absolute difference and CoV of difference with diastolic diameter, mean NCS, mean NRS, and mean NSS were assessed with multiple linear regression. Differences in interobserver coefficient of variation for manually segmented masks (variability in strain between observers) vs coefficient of variation for semiautomatically segmented masks (variability in strain between initial rough masks) were assessed using paired Student's t-test for each axial location. Statistical analysis was conducted in R (R Core Team, 2020. Vienna, Austria). Additionally, discrete Fréchet distances between the manual and automatically generated normalized circumferential, radial, and shear strain curves were computed to compare curve similarity on a non-sector-by-sector basis in MATLAB [82, 83].

3.3 Results

The semiautomatic segmentation technique generated masks adequate for strain analysis for all but one volunteer scan. Semiautomatically obtained NCS showed minimal sensitivity to the differences in initial rough mask, particularly in the PDA where the variability between semiautomatic runs was significantly lower than the variability between manual masks ($p < 0.05$) (Table 3.1). Overall, the mean absolute difference in normalized circumferential, radial, and shear strain between the manual and semiautomatic masks (determined as the mean of the magnitude of sector-by-sector differences in strain) was lowest in the PDA (0.556 ± 0.43), followed by the IAA (0.661 ± 0.44) and the DTA (0.838 ± 0.55) (Table 3.2). When looking at individual strain types,

the mean absolute difference in normalized strain between manual and semiautomatic masks was lowest for the NCS (0.224 ± 0.09), followed by the NSS (0.859 ± 0.39) and NRS (1.028 ± 0.47) (Table 3.2). For manual vs semiautomatic comparisons that are not explicitly governed by sector-by-sector comparisons, discrete Fréchet distances showed similar trends by strain type with NCS (0.565 ± 0.21) significantly outperforming NSS (1.763 ± 0.74, $p < 0.001$) and NRS (2.236 ± 1.13, $p < 0.001$) and by axial location with the PDA (1.256 ± 0.85) showing lower but not significant discrete Fréchet distances compared to the IAA (1.479 ± 1.04) and DTA (1.733 ± 1.15) (Table 3.2).

Kruskal-Wallis analysis of variance suggested no significant differences by axial location for mean absolute difference in normalized strain between manual and semiautomatic masks for NCS ($p = 0.266$), NRS ($p = 0.063$), or NSS ($p = 0.144$). However, when comparing differences in unnormalized circumferential strain by axial location, the mean absolute difference between manual and automatic segmentations in the IAA (0.007 ± 0.00) was significantly lower than the PDA (0.021 ± 0.01, $p < 0.01$) and the DTA (0.031 ± 0.01, $p < 0.001$). Comparisons between strain types for mean absolute difference in strain between manual and semiautomatic masks revealed a significant difference ($p < 0.001$) between NCS and both NRS and NSS ($p < 0.001$ for both) but no difference between NRS and NSS ($p = 0.412$). From multiple linear regression, mean absolute difference in strain between manual and semiautomatic masks was not significantly associated with mean NCS, NRS, or NSS, diastolic diameter, or sector-by-sector NCS CoV, NRS CoV, or NSS CoV.

Table 3.1: Comparisons of interobserver coefficient of variation (CoV) for manual segmentations (n=3 for IAA and PDA, n=2 for DTA) and for semiautomatic segmentations with different initial rough masks (n=2 for all volunteers) done with a two-tailed paired sample t-test for each axial location for the NCS.

	Manual Masks Mean CoV (±SD)	Semiautomatic Masks Mean CoV (±SD)	p-value
PDA	0.2444 ± 0.11	0.1682 ± 0.07	p = 0.017*
DTA	0.0975 ± 0.04	0.1348 ± 0.05	p = 0.07
IAA	0.2114 ± 0.06	0.2234 ± 0.10	p = 0.72

Table 3.2: The mean strain magnitude (manually generated), mean absolute difference in strain, coefficient of variation (CoV) of the differences in strain calculated using mean manual vs. mean semiautomated masks, and the percentage of total sectors with a normalized strain difference between the means of each method below 33% or unnormalized difference below 0.03%, and discrete Fréchet distance between normalized strain curves for each strain type at each axial aortic location.

		Mean Strain Mag. (Manual)	Norm. Mean Abs. Diff. (±SD)	CoV Mean Diff.	Sectors <33% Norm Strain Diff.	Sectors <0.03 Strain Diff.	Discrete Fréchet Dist. (±SD)
PDA (n = 8)	NCS	0.09	0.2280 ± 0.06	0.2640	75.8%	76.6%	0.6176 ± 0.19
	NRS	0.05	0.7854 ± 0.56	0.7162	41.4%	39.1%	1.6889 ± 1.02
	NSS	0.04	0.6546 ± 0.27	0.4173	28.9%	62.5%	1.4614 ± 0.66
DTA (n = 11)	NCS	0.14	0.2312 ± 0.07	0.3185	80.5%	49.0%	0.5709 ± 0.19
	NRS	0.05	1.2761 ± 0.35	0.2765	14.8%	21.4%	2.6702 ± 0.96
	NSS	0.04	1.0064 ± 0.43	0.4286	17.2%	30.7%	1.9591 ± 0.87
IAA (n = 10)	NCS	0.04	0.2131 ± 0.12	0.5830	73.1%	79.4%	0.5158 ± 0.24
	NRS	0.06	0.9232 ± 0.36	0.3951	24.4%	33.1%	2.1524 ± 1.20
	NSS	0.04	0.8471 ± 0.34	0.4048	25.0%	49.3%	1.7685 ± 0.52

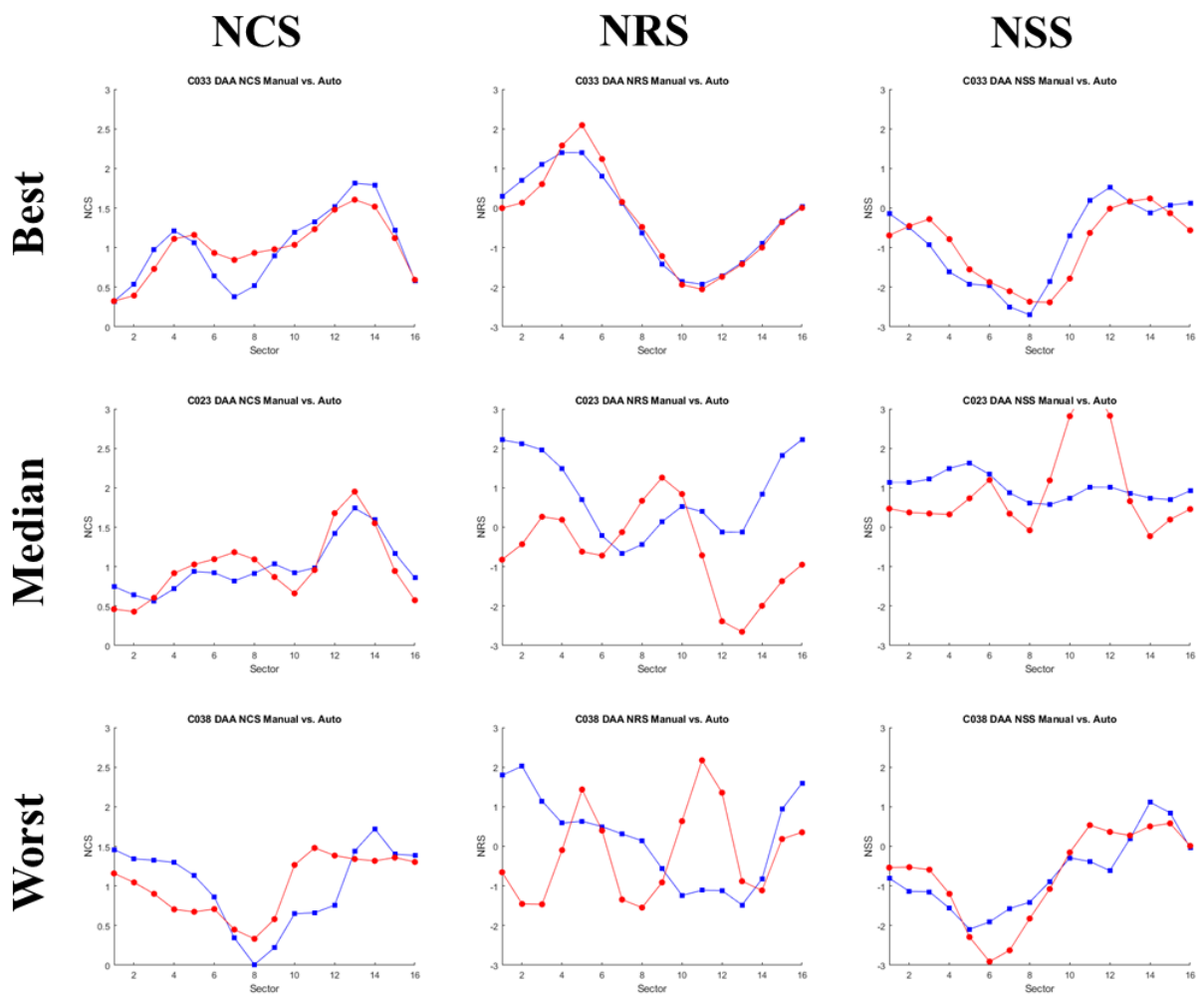

Figure 3.6: Manual (*blue*) vs semiautomatically calculated (*red*) NCS, NRS, and NSS for the best, median, and worst case (determined by mean absolute difference in NCS) for the proximal descending aorta.

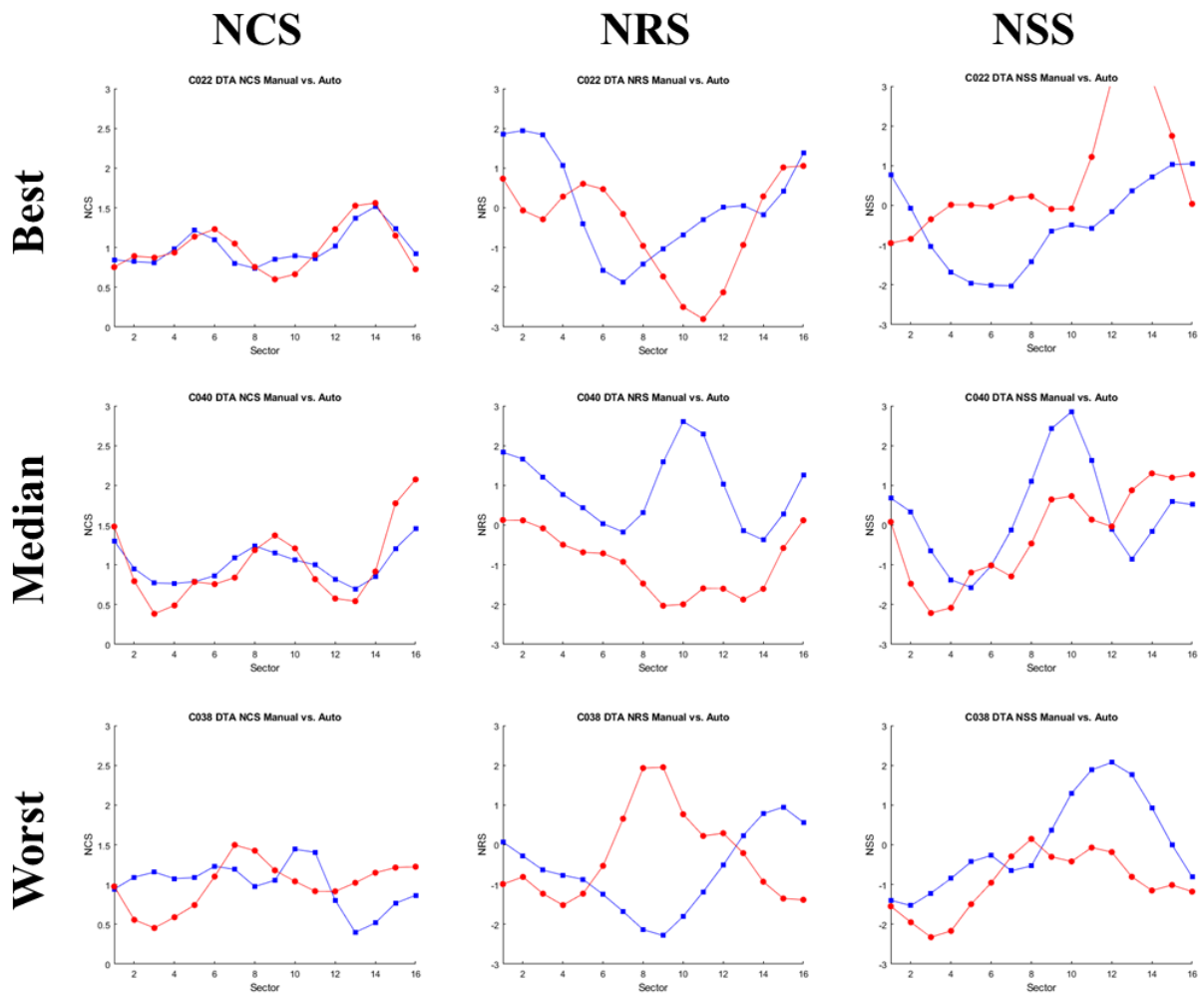

Figure 3.7: Manual (*blue*) vs semiautomatically calculated (*red*) NCS, NRS, and NSS for the best, median, and worst case (determined by mean absolute difference in NCS) for the mid-descending thoracic aorta.

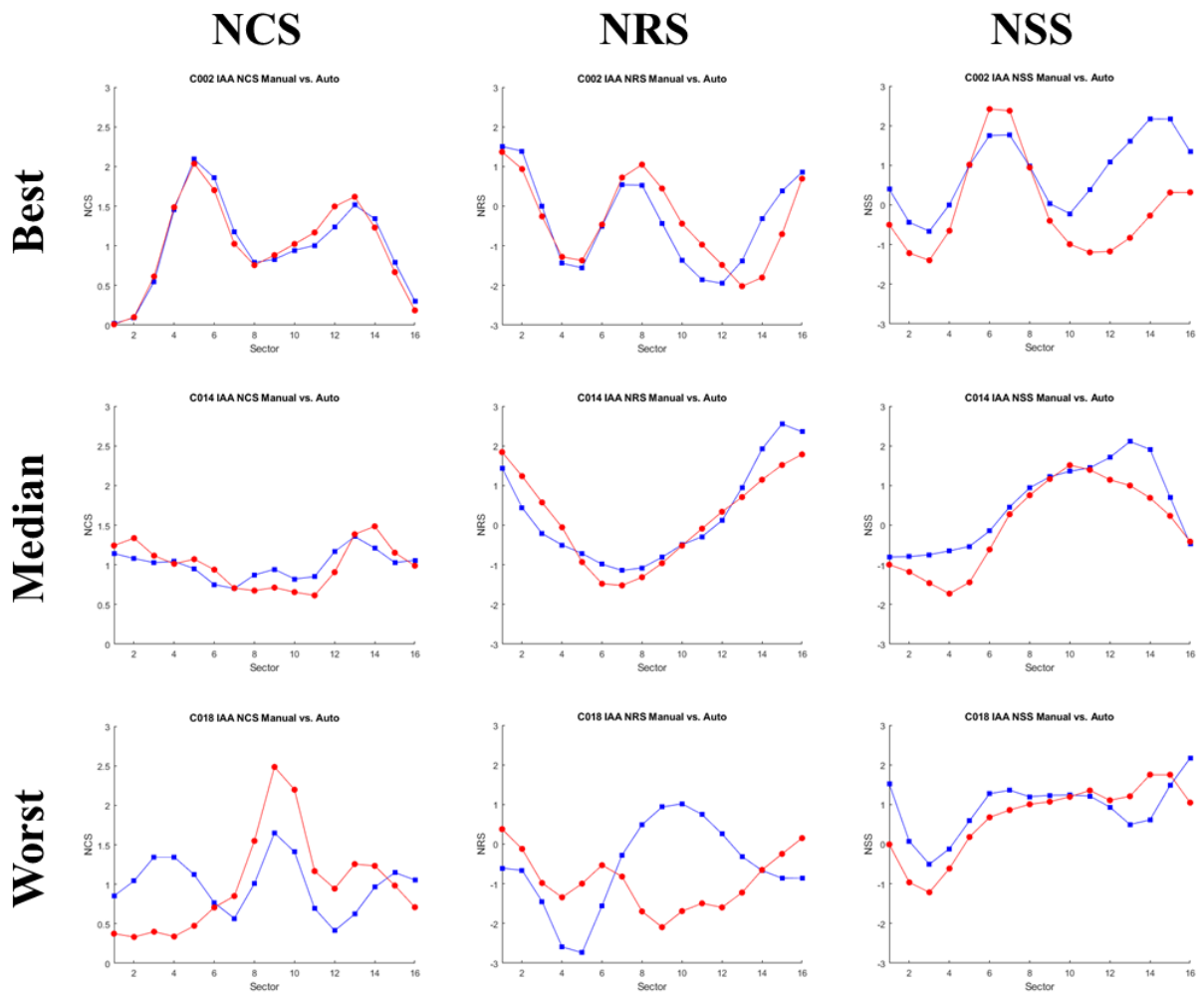

Figure 3.8: Manual (*blue*) vs semiautomatically calculated (*red*) NCS, NRS, and NSS for the best, median, and worst case (determined by mean absolute difference in NCS) for the infrarenal abdominal aorta.

3.4 Discussion

The semiautomatic segmentation method for aorta DENSE MRI greatly reduced the time required for segmentation from over an hour to under 10 minutes (including manual verification of automatically generated contours), while showing good agreement compared to the original manual method for the calculation of circumferential strain, with a mean strain difference of less than 0.033 for all locations studied. The method, based on the kinematic data output from the

DENSE sequence, takes advantage of strong differences between phase in voxels representing the aortic wall and voxels in the lumen or periadventitial areas. Additionally, by weighting the masks with the best tracked position vectors for each sector, the method was robust for removing edge voxels that had similar signal in an individual timeframe but did not track in the wall over time. The overall mean absolute difference in NCS (0.224 ± 0.09) between the manual and semiautomatic masks was comparable to the interobserver and intraobserver mean absolute differences in NCS reported in Chapter 2 (0.228 and 0.210, respectively).

There were no significant differences in mean absolute difference between semiautomatic masking and manual masking by axial locations. However, the variability in manual masks was lowest for the DTA compared to the PDA and IAA (Table 3.1), demonstrating lower overall differences between observers for the manual DTA mask segmentations while resulting larger average distances between the manual and semiautomatic masks. This may be due to the higher incidence of phase wrapping in the DTA, which can be considered manually but causes problems for the semi-automatic method since the calculated displacement for wrapped voxels will be incorrect and often of the opposite direction. Repeatability quantified by the mean coefficient of variation in NCS between manual observers or between semiautomatic runs was significantly better for the semiautomatic method in the PDA compared to the interobserver repeatability ($p < 0.05$), with no statistical differences in the IAA and DTA. This suggests that the variability in the semiautomatic method introduced by different rough masks was comparable or better than interobserver repeatability for this study, but additional investigations are needed to quantify fully the degree of sensitivity of the final semiautomatic masks to the initial rough masks.

The better agreement between semiautomatic and manual masks for NCS calculation compared to the NRS and NSS matched the general trends in interobserver and intraobserver

repeatability seen previously [81]. Due to the elimination of spatial smoothing between the inner and outer layers of the aortic wall, the effect of random noise and single outlier voxels included in each layer are not averaged out to the same degree as previously, leading to larger variation and potential errors in the strain calculation. As opposed to the circumferential direction in which the displacement of multiple neighboring voxels are smoothed and strains are measured across the width of an entire sector, this effect is magnified for radial and shear strain calculation since only two voxels are present in the radial direction through the aortic wall from which to calculate strain; therefore, the radial and shear calculations would benefit more from a single outlier voxel elimination.

Future improvements to this approach may include an additional filter step where a single voxel can be eliminated by comparing the magnitude and direction of the stepwise displacement to its neighboring voxels. Additionally, efforts are being made to reduce user variability of the semiautomatic masking algorithm through the use of traditional edge detection techniques to form the initial rough mask without user input. While the semiautomatic technique was robust to different initial mask starting points, the ability to automatically determine the region containing the wall with varying amounts of specificity (i.e., purposefully including more or fewer voxels of the lumen and adventitial space) should be further explored to quantify how much the initial mask affects the convergence of the final mask to the 'true' aortic wall.

The discrete Fréchet distance to measure the agreement between the manual and semiautomatically generated strain curves in addition to the mean absolute difference in strain was included to better assess curve similarity in cases where the curves had the same general shape with similar local maximum and minimum strain values but were offset horizontally (i.e., shifted by 1 or 2 sectors). In these situations, the sector-by-sector comparison of the two curves

overrepresents their differences and may not adequately capture physiologically relevant similarities in strain pattern. This situation is relatively rare and the trends of mean discrete Fréchet distance between axial locations and strain types for the full data set matched those determined by the mean absolute difference, but for individual cases the use of discrete Fréchet distance may be preferred.

The use of the raw displacement images for mask generation before any phase unwrapping was conducted is one limitation of this method. Correcting phase wrapping before calculating displacements for timepoint back-projection may improve the results, especially in the DTA where phase wrapping was the most common. Another limitation of this study was that the volunteers included were all from a healthy cohort with normal aortic mechanics. The inclusion of DENSE scans from patients with aortopathy such as in vessels with reduced compliance resulting in lower frame-to-frame displacements or with small focal heterogeneities displaying significantly different behavior than adjacent parts of the wall will need to be assessed to confirm applicability in patients with pathological aortic mechanics.

In conclusion, this semiautomatic approach to segmenting the aortic wall using the kinematic information from DENSE MRI greatly reduced the time that it takes to analyze aortic wall mechanics without overly impacting the NCS obtained. Differences between the semiautomatically calculated and manually calculated NCS was also comparable to interobserver and intraobserver differences within the manually generated NCS. While the NRS and NSS are more sensitive to outlier voxels and tend to have larger differences when comparing semi-automatically generated masks and manually generated masks, the inclusion of additional filtering steps could help to reduce those differences moving forward. Overall, this new semi-automatic technique may help to overcome the long analysis times for DENSE aortic strain imaging while

reducing the user-dependent error from manual masking to improve the potential clinical utility of DENSE MRI.

4 Assessment of Aortic Solid and Fluid Mechanics in Patients at Elevated Risk for Aortopathy Development

4.1 Introduction

Aortic dissections and aneurysms are vascular events associated with high mortality if left untreated, but this risk can be reduced with early diagnosis and management in the initial stages of development. Type B aortic dissections, or those originating in the descending aorta, account for 25-40% of all aortic dissections and are preferentially managed medically if diagnosed early unless there are clinical indications for immediate surgical repair [84, 85]. Many of these type B aortic dissections are diagnosed in the emergency department as acute events, rather than in the more chronic remodeling stages. For patients presenting with acute dissection, in-hospital mortality rates are as high as 27% for medical management, up to 18% for endovascular repair, and up to 17% for open surgical repair [3]. For aneurysms in the descending thoracic aorta, risk of rupture is clinically assessed currently based primarily on maximal aortic diameter and adequate distal perfusion without consideration of local fluid and tissue mechanics that may provide further patient-specific data to more accurately assess rupture-risk compared to the risk of intervention. Risks associated with both endovascular and open surgical repair of aneurysms and dissections demonstrate the need for accurate quantification of their stability for improved clinical decision-making [86].

However, in addition to quantifying the stability of existing aneurysms and dissections in the descending aorta, earlier assessment of aortic wall mechanics in patients with elevated risk of future aortopathy could allow for improved monitoring, potential preventative interventions, and improved long-term outcomes. Common risk factors for type B aortic dissection include

hypertension, atherosclerosis, and previous aortic aneurysms or dissection [87]. For aneurysms of the descending aorta, associated risk factors include hypertension and smoking, family history of aortopathies, and genetic syndromes including Marfan syndrome, Loeys-Dietz syndrome, Ehlers-Danlos Type IV (vascular form), and Turners syndrome [86, 88]. These syndromes are also associated with development of aortic aneurysm and dissection at earlier ages compared to other risk factors, and differences in outcomes in response to similar treatments.

The dysregulation of normal aortic remodeling in these syndromes often leads to accelerated vascular aging through increase in collagen content and loss of functional elastin, contributing to increased resistance to vessel deformation with pulsatile blood flow [89]. The deformation of the proximal descending aorta is necessary for the accommodation of the blood volume output by the heart. Without compensatory changes in cardiac output, these mechanical changes could contribute to elevated wall shear stress (WSS) and modified tissue strain characteristics [15, 90] . Changes in the magnitude or direction of WSS due to increased blood velocity or disturbed flow have been shown to drive endothelial cell phenotypic changes and increase remodeling behaviors that lead to aneurysmal progression [91, 92].

Quantification of the fluid and tissue mechanics in patients at elevated risk for developing aortopathies could improve the understanding of how vessel mechanics influence the occurrence and development of aneurysms and dissections of the descending aorta, and may reveal regional functional changes in the aorta before obvious and often permanent anatomical changes occur (e.g., dilation, dissection, etc.). Phase-contrast (PC) MRI (both 2D and 3D) has increasingly been utilized for cardiovascular flow analysis through highly reproducible quantification of blood velocity fields and quantification of related metrics such as wall shear stress at the endothelial surface [93, 94]. Additionally, the use of aortic DENSE MRI for measurement of heterogeneities

in circumferential, radial, and shear strains in the aortic wall itself has been evaluated in healthy cohorts, with promising results [20, 45, 81]. In this preliminary study, DENSE MRI will be used to quantify the strain magnitudes and patterns present in the proximal descending aorta in healthy volunteers compared to patients with hypertension or Marfan syndrome, both of which are at elevated risk of aortopathy. Additionally, the inclusion of fluid mechanical analysis with 4D flow at the same locations as tissue mechanical quantification via DENSE MRI will allow for direct regional correlation of fluid flow, flow-induced wall shear stress, and aortic wall tissue strain.

4.2 Methods

Imaging: Following approval by the Virginia Commonwealth University Institutional Review Board, one healthy patient without a history of aortopathy or hypertension and two patients with documented hypertension or Marfan syndrome underwent non-contrast MR imaging of the aorta on a 3T Siemens Skyra scanner (Siemens Healthineers, Erlangen, Germany). Cine DENSE MR images were acquired in the proximal descending aorta distal to the left subclavian artery, oriented normally to the longitudinal direction of the aorta. DENSE imaging parameters included 1.3 x 1.3 x 8 mm voxel dimension, TR 16 ms, TE 1.21 ms, flip angle 15 degrees, 0.17 cyc/mm in plane displacement encoding frequency, and spiral k-space sampling with 18 spiral interleaves and 4 signal averages. DENSE image acquisition time was approximately 8-10 minutes.

4D flow PC-MR cine images were acquired in the left anterior oblique orientation to include the full aortic arch and proximal descending aorta distally to the renal artery. 4D-flow imaging parameters included velocity encoding of 150 cm/sec, 2.5 x 2.5 x 2.5 mm spatial resolution, 38 ms temporal resolution, with prospective ECG and respiratory navigator gating. Image acquisition time was approximately 8 minutes.

Post-processing: All postprocessing of cine DENSE MR images was performed in MATLAB (Mathworks, Natick, MA) as previously described in Jones and Wilson, 2021 [81]. Following manual mask segmentation and calculation of circumferential, radial, and shear strains, all masks were aligned based on the most posteriorly located sector. Post-processing of 4D flow cine images was performed in Caas MR 4D Flow (Pie Medical Imaging, Maastricht, Netherlands) per vendor instructions to obtain wall shear stress (WSS) and wall normal stress (WNS) measurements for 90 points around the endothelial boundary of the aortic lumen in six sequential analysis planes manually positioned distal to the left subclavian artery and normal to the longitudinal axis of the aorta. The multiple analysis planes were used to address limitations arising from current lack of registration of DENSE imaging plane position and 4D flow analysis plane position, as well as to adequately capture local longitudinal changes in wall stress measurements at the level of DENSE wall mechanics measurements. These stress outputs were further processed in MATLAB to orient by the most posteriorly located point and divided into sectors matching those of the DENSE strain maps. The 4D flow analysis planes most closely aligned with the DENSE imaging plane were selected manually. WSS and WNS were normalized by their mean magnitude, and flow patterns were assessed and compared to normalized circumferential strain in the aortic wall from DENSE MRI.

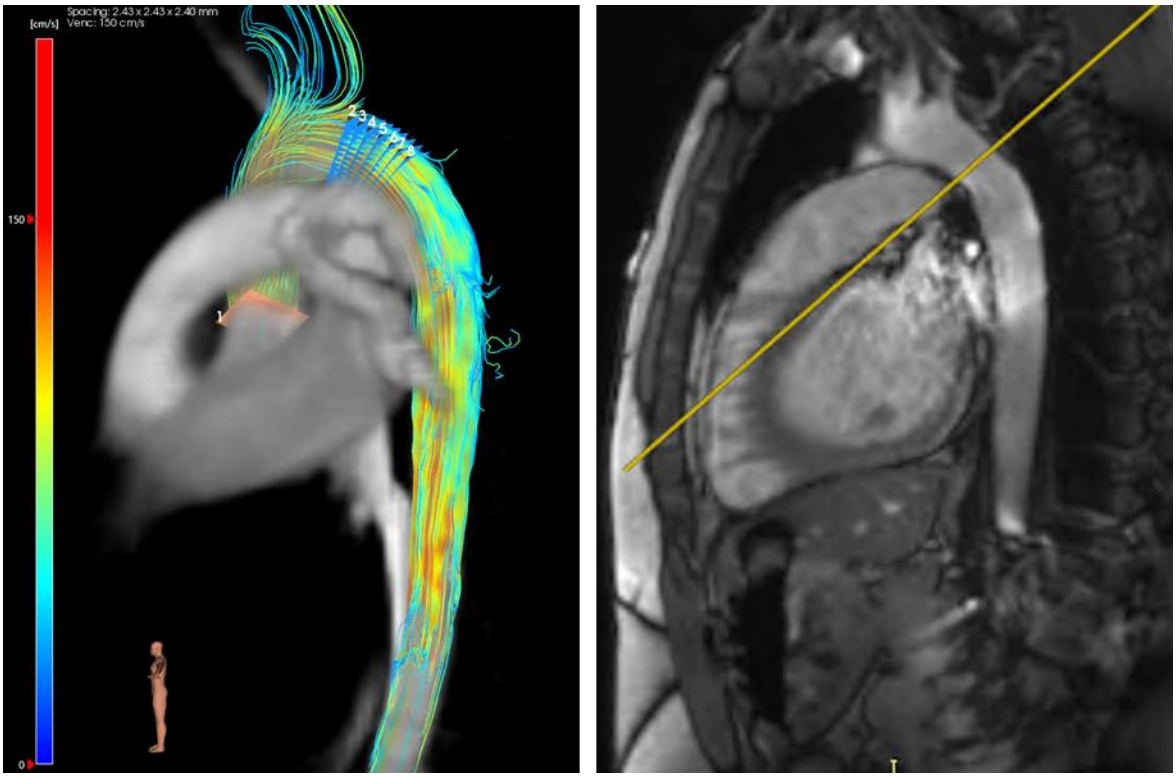

Figure 4.1: (*Left*) flow streamlines output from Caas MR 4D Flow analysis. (*Right*) Sagittal FISP MR image of the thoracic aorta with the DENSE image plane marked as a yellow segment for manual alignment of the 4D flow analysis planes.

4.3 Results

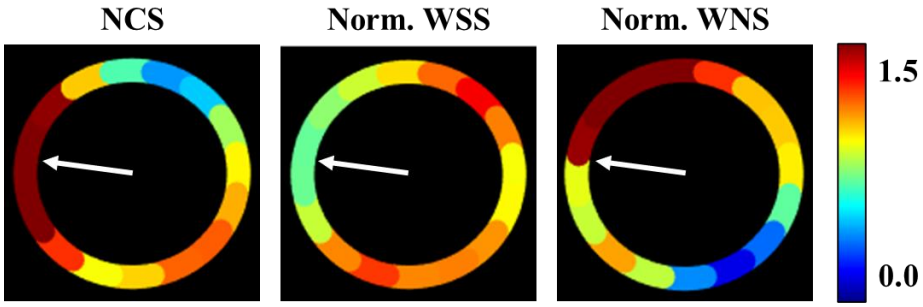

Figure 4.2: Normalized circumferential strain (left), normalized wall shear stress (middle), and normalized wall normal stress (right) for volunteer with no history of aortopathy or hypertension. The arrow indicates the greater curvature of the aortic arch.

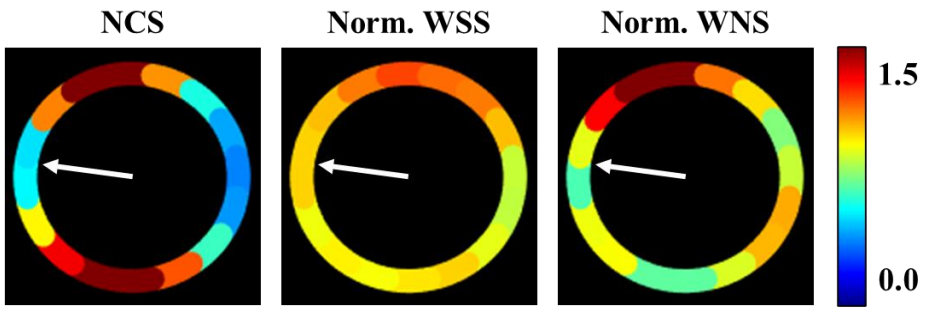

Figure 4.3: Normalized circumferential strain (*left*), normalized wall shear stress (*middle*), and normalized wall normal stress (*right*) for volunteer with hypertension. The arrow indicates the greater curvature of the aortic arch.

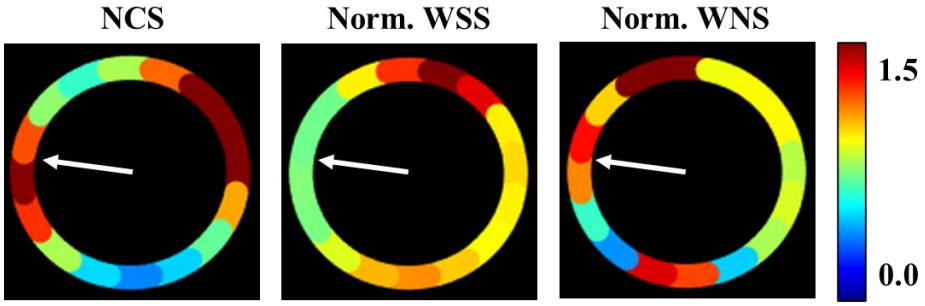

Figure 4.4: Normalized circumferential strain (left), normalized wall shear stress (middle), and normalized wall normal stress (right) for volunteer with Marfan syndrome. The arrow indicates the greater curvature of the aortic arch.

4.4 Discussion

It is impossible to draw any conclusions from the sample size available to date in this small pilot, but some observations regarding patterns in stress and strain distributions are noted. The normalized WSS distributions were similar between all three volunteers, with peak values occurring along the lateral side of the aorta between the greater and lesser curvature. This is not unexpected that the WSS would be higher in this region as the flow leaving the ascending aorta is projected into the top of the curvature of the arch and follows it around to the proximal descending aorta. From this limited data, there also appears to be a tendency for normalized WNS to be highest

along the lateral side of the greater curvature of the aorta. One interesting pattern to consider from the normalized WNS maps is the general smoothness of transitions for the healthy volunteer and volunteer with hypertension from a single region of peak values around the lateral greater curvature. This contrasts with the volunteer with Marfan syndrome, where there was a notably less consistent pattern with several local minimums and maximums along the greater curvature between the lateral and medial portions. Both the location of the peak normalized wall stress values and the variability of stress distributions will be considered in future volunteers. While the small sample size in this pilot study prevents the drawing of any broad conclusions between patients or between fluid and solid mechanics, the ability to quantify regional wall shear stress at the luminal border of the aorta in addition to strain in the wall itself grants a promising new approach to assessing and correlating the complex mechanics present in the proximal descending aorta.

The analysis of 4D flow data sets following acquisition to obtain WSS and WNS maps is simple and straightforward, but reliant on manually positioning planes of interest along the aorta. Attempts were made to better represent the WSS and WNS present at the same axial position as the DENSE images by averaging together planes on either side of the apparent DENSE imaging location, but this technique may introduce error, especially in the presence of any small focal heterogeneities in shear along the axial direction of the aorta. Additionally, the orientation of the normalized WSS and WNS plots against the orientation of the NCS plots was done by taking the most posterior point present in each cross-section and rotating all plots such that the selected point was aligned. With the complex curvature of the aorta present in the arch and proximal descending portions, this could result in some degree of error when aligning the DENSE and 4D flow measures for comparison. An improved registration method that can align the DENSE imaging plane

automatically with the 4D flow data to extract WSS and WNS measurements at the exact level of wall strain measurements would likely benefit the repeatability of this process.

In addition to looking at flow-induced shear stresses at the luminal aortic border, the use of the velocity profiles derived directly from the PC-MRI data presents another avenue for exploring the relationships between fluid behaviors and the risk of developing aortopathy. Quantifying measures such as variability of flow magnitude and direction along a given part of the wall would make it possible to assess the oscillatory behavior of flow, which may be related to endothelial cell phenotype/dysfunction and extracellular matrix remodeling in different portions of the aortic wall. Overall, the development of this method coupling DENSE tissue strain analysis with 4D flow wall shear stress analysis represents an important step towards fully quantifying aortic mechanics. However, more studies must be conducted to assess if there are any differences between healthy controls and patients at elevated risk of developing aortopathies, and if so how those measured differences in wall strain, WSS, and WNS may contribute to early focal changes in the formation of dissections and aneurysms.

5 Conclusion

The use of non-invasive MRI techniques to quantify the mechanics in the descending aorta offers a promising toolset for the study of the pathogenesis of aortopathy. The work discussed in this thesis details recent efforts to improve DENSE MRI analysis by fully quantifying the 2D cylindrical strain tensor and reducing the lengthy post-processing time through semi-automatic segmentation of aortic wall masks. Additionally, developing a data-processing pipeline for regionally correlating fluid mechanical metrics derived from 4D flow MRI to aortic wall strain by DENSE MRI offers a promising new tool for evaluating aortic mechanics. Together, the coupled analysis of luminal fluid mechanics and wall tissue mechanics in patients at elevated risk of developing aneurysms and dissections could uncover the contribution of mechanics to the initial stages of dissection via intimal tear and medial infiltration or early aortic dilatation in aneurysmal formation. Additionally, future use of these techniques to assess stability in patients with existing pathology will help to better inform clinicians when deciding which course of treatment or intervention to pursue.

In the first part of this thesis, a new method for aortic DENSE post-processing was introduced. The spatial smoothing component of DENSE analysis, which previously involved averaging displacement vectors with nearby neighbors to reduce the noise present, was modified such that spatial averaging was done discretely for the inner and outer layers of displacement vectors in the aortic wall mask. The differences in displacement between these two layers is necessary to quantify radial strain by the compression or spreading apart of these two layers and shear strain by the relative differences in translation of the two layers in the circumferential direction. The updated analysis was performed on 32 aortic cross-section cine DENSE image sets from three axial locations in a healthy patient cohort, yielding preserved radial and shear strain

measurements with minimal impacts on the calculation of the circumferential strain. Like the circumferential strain, the distribution of radial and shear strains was heterogenous around the aortic circumference, and there appeared to be differences by patient age, though additional studies must be conducted to fully assess this possibility. Future studies are also needed to assess any differences in aortic wall mechanics in patients with hypertension, connective tissue disorders, or existing aortopathy that may indicate elevated risk of acute aortic events.

One of the primary limitations of aortic mechanical analysis from DENSE MRI however is the reliance on manual segmentation, which is time-intensive and limits the repeatability of strain measurement. The second aim of this work was to automate most or all the post-processing pipeline to improve clinical utility through reduced analysis times and improved repeatability. The method developed and described in Chapter 3 was dependent on the kinematic data in the form of DENSE-derived displacements. By taking advantage of this unique property of DENSE MRI, it was possible to automatically reduce broad initial starting regions down to the luminal and adventitial borders of the aortic wall in minutes rather than taking over an hour per scan. The semiautomatic method showed good agreement with the manually calculated NCS, with lower internal variability between masks generated from different starting regions compared to interobserver variability in the PDA, and with no significant differences in the DTA and IAA. The agreement in NRS and NSS between the manual and semiautomatic methods was significantly lower, likely due to the increased sensitivity to noise and individual outlier voxels. Future improvements including single voxel elimination and automatically setting the initial starting regions are currently underway and are expected to further increase repeatability of the automatic post-processing method. Further evaluation of the automatic method, however, is also needed to assess its performance in patients with abnormal anatomy or aortic mechanics due to pathology.

The third focus of this work was to begin applying DENSE analysis in patients at elevated risk of aortopathies alongside 4D flow MRI to study the relationships between fluid and solid tissue mechanics in the proximal descending aorta. Unfortunately, the many barriers faced over the past two years from both efforts to mitigate the spread of COVID-19 and unexpected hurdles in acquiring, installing, and receiving permission to use new research MRI sequences in a clinical setting pushed back the original timelines for new data collection. Consequently, at the time of this thesis only three data collection sessions have successfully produced adequate DENSE and 4D flow MR image sets for combined analysis and comparison. While not ideal, this has still allowed for the development of the analysis pipeline. Between the new semiautomatic segmentation algorithm for DENSE and straightforward 4D flow analysis in vendor software with automatic post-processing in MATLAB, the process between image acquisition and assessment of relationships between fluid and tissue mechanics has become streamlined. Further developments are underway and ongoing to better integrate analysis of data from the two imaging sources, with the goal to eventually build a fully functional, user-interface driven processing tool.

References

[1] O. Khavjou, D. Phelps and A. Leib, "Projections of Cardiovascular Disease Prevalence and Costs: 2015–2035," American Heart Association, Washington, DC, 2016.

[2] M. Landenhed, G. Engstrom, A. Gottsater, M. Caulfield, B. Hedblad and C. Newton-Cheh, "Risk profiles for aortic dissection and ruptured or surgically treated aneurysms: a prospective cohort study," *J Am Heart Assoc,* vol. 4, no. 1, 2015.

[3] F. Mussa, J. Horton, R. Moridzadeh, J. Nicholson, S. Trimarchi and K. Eagle, "Acute aortic dissection and intramural hematoma: a systematic review," *JAMA,* vol. 316, no. 7, pp. 754-763, 2016.

[4] J. Moxon, A. Parr, T. Emeto, P. Walker, P. Norman and J. Golledge, "Diagnosis and monitoring of abdominal aortic aneurysm:," *Curr Probl Cardiol,* vol. 35, no. 10, pp. 512-548, 2010.

[5] R. Davies, L. Goldstein, M. Coady, S. Tittle, J. Rizzo, G. Kopf and J. Elefteriades, "Yearly Rupture or Dissection Rates for Thoracic Aortic Aneurysms: Simple prediction based on size," *Ann Thorac Surg,* vol. 73, pp. 17-28, 2002.

[6] J. Kim, K. Kim, M. Lindsay, T. MacGallivray, E. Isselbacher, R. Cambria and T. Sundt, "Risk of Rupture or Dissection in Descending," *Circulation,* vol. 132, pp. 1620-1629, 2015.

[7] G. Hurlock, H. Higashino and T. Mochizuki, "History of cardiac computed tomography: Single to 320-detector row multislice computed tomography," *Int J Cardiovasc Imaging,* vol. 25, pp. 31-42, 2009.

[8] R. Meyer, "History of Ultrasound in Cardiology," *J Ultrasound Med,* vol. 23, no. 1, pp. 1-11, 2004.

[9] G. Pohost, "The History of Cardiovascular Magnetic Resonance," *JACC: Cardiovascular Imaging,* vol. 1, no. 5, pp. 672-678, 2008.

[10] N. McAlister, N. McAlister and K. Buttoo, "Understanding cardiac "echo" reports: Practical guide for referring physicans," *Canadian Family Physicians,* vol. 52, pp. 869-874, 2006.

[11] S. Battaglia, G. Danesino, V. Danesino and S. Castellani, "Color Doppler ultrasonography of the abdominal aorta," *Journal of Ultrasound,* vol. 13, pp. 107-117, 2010.

[12] J. J. Park, J.-B. Park, J.-H. Park and G.-Y. Cho, "Global Longitudinal Strain to Predict Mortality in Patients With Acute Heart Failure," *Journal of the American Collge of Cardiology,* vol. 71, no. 18, pp. 1947-1957, 2018.

[13] Y. C. Fung, Biomechanics: Mechanical Properties of Living Tissues, New York, NY: Springer-Veerlag, 1993.

[14] C. Jacobs, H. Huang and R. Kwon, Introduction to Cell Mechanics and Mechanobiology, New York, NY: Garland Science, Taylor & Francis Group, LLC, 2013.

[15] G. Kassab, "Biomechanics of the cardiovascular system: the aorta as an illustratory example," *J R Soc Interface,* vol. 3, no. 11, pp. 719-740, 2006.

[16] B. M. Kaess, J. Rong, M. Larson, N. Hamburg, J. Vita, D. Levy, E. Benjamin, R. Vasan and G. Mitchell, "Aortic stiffness, blood pressure progression, and incident hypertension," *JAMA,* vol. 308, no. 9, pp. 875-881, 2012.

[17] Y. Fung, S. Liu and J. Zhou, "Remodeling of the constitutive eqution while a blood vessel remodels itself under stress," *Journal of Biomechanical Engineering,* vol. 115, pp. 453-459, 1993.

[18] J. Bracamonte, J. Wilson and J. Soares, "Assessing Patient-Specific Mechanical Properties of Aortic Wall and Peri-Aortic Structures From In Vivo DENSE Magnetic Resonance Imaging Using an Inverse Finite Element Method and Elastic Foundation Boundary Conditions," *Journal of Biomechanical Engineering,* vol. 142, no. 12, 2020.

[19] J. D. Humphrey and S. L. O'Rourke, An Introduction to Biomechanics: Solids and Fluids, Analysis and Design, New York, NY: Springer Science+Business Media, 2015.

[20] J. Wilson, X. Zhong, J. Hair, W. Taylor and J. Oshinksi, "In Vivo Quantification of Regional Circumferential Green Strain in the Thoracic," *J. Biomech. Eng,* vol. 141, no. 6, 2018.

[21] B. Hoit, "Strain and strain rate echocardiography and coronary artery disease," *Circulation: Cardiovascular Imaging,* vol. 4, pp. 179-190, 2011.

[22] M. Dandel, H. Lehmkuhl, C. Knosalla, N. Suramelashvili and R. Hetzer, "Strain and strain rate imaging by echocardiography - basic concepts and clinical applicability," *Current Cardiology Reviews,* vol. 5, pp. 133-148, 2009.

[23] G. Perk, P. Tunick and I. Kronzon, "Non-Doppler Two-dimensional Strain Imaging by Echocardiography - From technical considerations to clinical applications," *Journal of the American Society of Echocardiography,* vol. 20, no. 3, pp. 234-243, 2007.

[24] D. Oxborough, A. Batterham, R. Shave, N. Artis, K. Birch, G. Whyte, P. Ainslie and K. George, "Interpretation of two-dimensional and tissue Doppler-derived strain and strain rate data: is there a need to normalize for individual variability in left ventricular morphology?," *European Journal of Echocardiography,* vol. 10, pp. 677-682, 2009.

[25] A. Schuster, K. Hor, J. Kowalick, P. Beerbaum and S. Kuty, "Cardiovascular magnetic resonance myocardial feature tracking: Concepts and clinical applications," *Advances in cardiovascular imaging,* vol. 9, no. 4, 2016.

[26] M. Sardana, P. Konda, Z. Hashmath, G. Oldland, S. Gaddam, R. Miller, V. Satija, B. Ansari, J. Lee, A. Mustafa, S. Akers and J. Chirinos, "Usefulness of Left Ventricular Strain by Cardiac Magnetic Resonance Feature-Tracking to Predict Cardiovascular Events in Patients With and Without Heart Failure," *Am J Cardiol,* vol. 123, no. 8, pp. 1301-1308, 2019.

[27] A. Kempny, R. Fernandex-Jimenez, S. Orwat, P. Schuler, A. Bunck, D. Maintz, H. Baumgartner and G.-P. Diller, "Quantification of biventricular myocardial function using cardiac magnetic resonance feature tracking, endocardial border delineation and echocardiographic speckle tracking in patients with repaired tetralogy of fallot and healthy controls," *Journal of Cardiovascular Magnetic Resonance,* vol. 14, no. 32, 2012.

[28] A. Scatteia, A. Baritussio and C. Bucciarelli-Ducci, "Strain imaging using cardiac magnetic resonance," *Heart Fail Rev,* vol. 22, pp. 465-476, 2017.

[29] T. Chitiboi and L. Axel, "Magnetic resonance imaging of myocardial strain: a review of current approaches," *Journal of Magnetic Resonance Imaging,* vol. 46, pp. 1263-1280, 2017.

[30] M. Shehata, S. Cheng, N. Osman, D. Bluemke and J. Lima, "Myocardial tissue tagging with cardiovascular magnetic resonance," *Journal of Cardiovascular Magnetic Resonance,* vol. 11, no. 1, 2009.

[31] M. Amzulescu, M. De Creane, H. Langet, A. Pasquet, D. Vancraeynest, P. A, J. Vanovershelde and B. Gerber, "Myocardial strai imaging: a review of general principles, validation, and sources of discrepancies," *Eur Heart J Cardiovasc Imaging,* vol. 20, no. 6, pp. 605-619, 2019.

[32] L. Wu, T. Germans, A. Guclu, M. Heymans, C. Allaart and A. van Rossum, "Feature tracking compared with tissue tagginf measruements of segmental strain by cardiovascular magnetic resonance," *Journal of Cardiovascular Magnetic Resonance,* vol. 16, no. 10, 2014.

[33] G. Korosoglou, S. Giusca, N. Hofmann, A. Patel, T. Lapinskas, B. Pieske, H. Steen, H. Katus and S. Kelle, "Strain-encoded magnetic resonance: a method for assessment of myocardial deformation," *ESC Heart Failure,* vol. 6, pp. 584-602, 2019.

[34] M. Neizel, D. Lossnitzer, G. Korosoglou, T. Schaufele, A. Lewien, H. Steen, H. Katus, N. Osman, Giannitsis and Evangelos, "Strain-encoded (SENC) magnetic resonance imaging to evaluate regional heterogeneity of myocardial strain in healthy volunteers: Comparison with conventional tagging," *J Magn Reson Imaging,* vol. 29, no. 1, pp. 99-105, 2009.

[35] B. Jung, M. Markl, D. Foll and J. Hennig, "Investigating myocardial motion by MRI using tissue phase mapping," *European Journal of Cardio-thoracic Surgery,* vol. 295, pp. 150-157, 2006.

[36] S. Petersen, B. Jung, F. Weismann, J. Selvanayagam, J. Francis, J. Hennig, S. Neubauer and M. Robson, "Myocardial tissue phase mapping with cine phase-contrast MR imaging: reigonal wall motion analysis in healthy volunteers," *Radiology,* vol. 238, no. 3, pp. 816-826, 2006.

[37] M. Draney, R. Herfkens, T. Hughes, N. Pelc, K. Wedding, C. Zarins and C. Taylor, "Quantification of vessel wall cyclic strain using cine phase contrast magnetic resonance imaging," *Annals of Biomedical Engineering,* vol. 30, pp. 1033-1045, 2002.

[38] M. Draney, F. Arko, M. Alley, M. Markl, R. Herfkens, N. Pelc, C. Zarins and C. Taylor, "Quantification of Vessel Wall Motion and Cyclic Strain," *Magnetic resonance in medicine,* vol. 52, pp. 286-295, 2004.

[39] G. McGinley, B. Bendiksen, L. Zhang, J. Aronsen, E. Norden, I. Sjaastad and E. Espe, "Accelerated magnetic resonance imaging tissue phase mapping of the rat myocardium using compressed sensing with iterative soft-thresholding," *PLoS ONE,* vol. 14, no. 7, 2019.

[40] A. Aletras, S. Ding, R. Balaban and H. Wen, "DENSE: Displacement encoding with stimulated echoes in cardiac functional MRI," *J Magn Reson,* vol. 137, no. 1, pp. 247-252, 1999.

[41] B. Spottiswoode, X. Zhong, A. Hess, C. Kramer, E. Meintzes, B. Mayosi and F. Epstein, "Tracking myocardial motion from cine DENSE images using spatiotemporal phase unwrapping and temporal fitting," *IEEE Transactions on Medical Imaging,* vol. 26, no. 1, pp. 15-30, 2007.

[42] J. Cao, N. Ngai, L. Duncanson, J. Cheng, K. Gliganic and Q. Chen, "A comparision of both DENSE and feature tracking techniques with tagging for the cardiovascular magnetic resonance assessment of myocardial strain," *Journal of Cardiovascular Magnetic Resonance,* vol. 20, no. 26, 2018.

[43] A. Young, B. Le, R. Kirton and B. Cowan, "Generalized spatiotemporal myocardial strain analysis for DENSE and SPAMM imaging," *Magnetic Resonance in Medicine,* vol. 67, pp. 1590-1599, 2012.

[44] K. Lin, L. Meng, J. Collins, V. Chowdhary, M. Markl and J. Carr, "Reproducibility of cine displacement encoding with stimulated echoes (DENSE) in human subjects," *Mangetic Resonance Imaging,* vol. 35, pp. 148-153, 2017.

[45] J. S. Wilson, W. Taylor and J. Oshinski, "Assessment of the regional distribution of nromalized circumferential strain in the thoracic and abdominal aorta using DENSE cardiovascular magnetic resonance," *Journal of Cardiovascular Magnetic Resonance,* vol. 21, no. 59, 2019.

[46] A. Cocciolone, J. Hawes, M. Staiculescu, E. Johnson, M. Murshed and J. Wagenseil, "Elastin, arterial mechanics, and cardiovascular disease," *Am J Physiol Heart Circ Physiol,* vol. 315, no. 2, pp. 189-205, 2018.

[47] W. Derwich, A. Wittek, K. Pfister, K. Nelson, J. Bereiter-Hahn, C. Fritzen, C. Blase and T. Schmitz-Rixen, "High resolution strain analysis comparing aorta and abdominal aortic aneurysm with real time three dimensional speckle tracking ultrasound," *Eur J Vasc Endovasc Surg,* vol. 51, no. 2, pp. 187-193, 2016.

[48] K. Karatolios, A. Wittek, T. Nwe, P. Bihari, A. Shelke, D. Josef, T. Schmitz-Rixen, J. Geks, B. Maisch, C. Blase, R. Moosdorf and S. Vogt, "Method for artic wall strain measurement with three-dimensional ultrasound speckle tracking and fitted finite element analysis," *Ann Thorac Surg,* vol. 96, no. 5, pp. 1664-1671, 2013.

[49] H. de Hoop, N. Petterson, F. van de Vosse, M. van Sambeek, H. Schwab and R. Lopata, "Multiperspective ultrasound strain imaging of the abdominal aorta," *IEEE Trans Med Imaging,* vol. 39, no. 11, pp. 3714-3724, 2020.

[50] M. Scarabello, M. Codari, F. Secchi, P. Cannao, M. Ali, G. Di Leo and F. Sardanelli, "Strain of ascending aorta on cardiac magnetic resonance in 1027 patients: relation with age, gender, and cardiovascular disease," *Eur J Radiol,* vol. 99, pp. 34-39, 2018.

[51] K. Wedding, M. Draney, R. Herfkens, C. Zarins, C. Taylor and N. Pelc, "Measurement of vessel wall strain using cine phase contrase MRI," *J Magn Reson Imaging,* vol. 15, no. 4, pp. 418-428, 2002.

[52] V. Ramanath, J. Oh, T. Sundt III and K. Eagle, "Acute aortic syndromes and thoracic aortic aneurysms," *Mayo Clinic Proceedings,* vol. 84, no. 5, pp. 465-481, 2009.

[53] J. Humphrey, Cardiovascular solid mechanics: cells, tissues, and organs, New York: Springer, 2002.

[54] D. Patel, D. Fry and J. Janicki, "Longitudinal tethering of arteries in dogs," *Circ Res,* vol. 19, no. 6, pp. 1011-1021, 1966.

[55] S. Hodis and M. Zamir, "Arterial wall tehtering as a distant boundary condition," *Phys Rev E,* vol. 80, no. 5, 2009.

[56] N. Petterson, E. van Disseldorp, M. van Sambeek, F. van de Vosse and R. Lopata, "Including surrounding tissue improves ultrasound-based 3D mechanical characterization of abdominal aortic aneurysms," *J Biomech,* vol. 85, pp. 126-133, 2019.

[57] C. Goergen, B. Johnson, J. Greve, C. Taylor and C. Zarins, "Increased anterior abdominal aortic wall motion: possible role in aneurysm pathogenesis and design of endovascular devices," *J Endovasc Ther,* vol. 14, no. 4, pp. 574-584, 2007.

[58] R. DeSanctis, R. Doroghazi, W. Austen and M. Buckley, "Aortic dissection," *N Engl J Med,* vol. 317, no. 17, pp. 1060-1067, 1987.

[59] M. Benjamin and W. Roberts, "Fatal aortic rupture from non-penetrating chest trauma," *Proc (Baylor Univ Med Cent),* vol. 25, no. 2, pp. 121-123, 2012.

[60] D.-Y. Huang and C.-H. Wang, "Optimal multi-level thresholding using a two-stage Otsu optimization approach," *Pattern Recognition Letters,* vol. 30, no. 3, pp. 275-284, 2009.

[61] L. Wang, T. Chitiboi, H. Meine, M. Gunther and H. K. Hahn, "Principles and methods for automatic and semi-automatic tissue segmentation in MRI data," *Magnetic Resonance Materials in Physics, Biology and Medicine,* vol. 29, no. 2, pp. 95-110, 2016.

[62] A. Zotin, K. Simonov, M. Kurako, Y. Hamad and S. Kirillova, "Edge detection in MRI brain tumor images based on fuzzy C-means clustering," *Preocedia Computer Science,* vol. 126, pp. 1261-1270, 2018.

[63] M. Lynch, O. Ghita and P. Whelan, "Automatic segmentation of the left ventricle cavity and myocardium in MRI data," *Computers in Biology and Medicine,* vol. 36, pp. 389-407, 2006.

[64] N. Sharma and L. Aggarwal, "Automated medical image segmentation techniques," *Journal of Medical Physics,* vol. 35, no. 1, pp. 3-14, 2010.

[65] M. Uzumucu, R. van der Geest, C. Swingen, J. Reiber and B. Lelieveldt, "Time Continuous Tracking and Segmentation of Cardiovascular Magnetic Resonance Images Using Multidimensional Dynamic Programming," *Investigative Radiology,* vol. 41, no. 1, pp. 52-62, 2006.

[66] D. Mahapatra, "Cardiac Image Segmentation from Cine Cardiac MRI Using Graph Cuts and Shape Priors," *Journal of Digital Imaging,* vol. 26, no. 4, pp. 721-730, 2013.

[67] J. Liu, X. Zhuang, H. Xie, S. Zhang and L. Gu, "Myocardium segmentation from DE MRI with guided random walkds and sparse shape representation," *International Journal of Cumputer Assisted Radiology and Surgery,* vol. 13, pp. 1579-1590, 2018.

[68] Y. Wang, Y. Zhang, W. Xuan, E. Kao, P. Cao, B. Tian, K. Ordovas, D. Saloner and J. Liu, "Fully automatic segmentation of 4D MRI for cardiac functional measurements," *Medical Physics,* vol. 46, no. 1, pp. 180-189, 2019.

[69] C. Nambakhsh, J. Yuan, K. Punithakumar, A. Goela, M. Majchl, T. Peters and I. Ayed, "Left ventricle segmentation in MRI via convex relaxed distribution matching," *Medical Image Analysis,* vol. 17, pp. 1010-1024, 2013.

[70] T. Kurzendorfer, C. Forman, M. Schmidt, C. Tillmanns, A. Maier and A. Brost, "Fully automatic segmentation of the left ventricle anatomy in 3-D LGE-MRI," *Computerized Medical Imaging and Graphics,* vol. 59, pp. 13-27, 2017.

[71] L. Xie, Y. Song and Q. Chen, "Automatic left ventricle segmentation in short-axis MRI using deep convolutional neural networks and central-line guided level set approach," *Computers in Biology and Medicine,* vol. 122, 2020.

[72] O. Bernard, "Deep Learning Techniques for Automatic MRI Cardiac Multi-Structures Segmentation and Diagnosis: Is the Problem Solved?," *IEEE Transactions on Medical Imaging,* vol. 37, no. 11, pp. 2514-2525, 2018.

[73] D. Vigneault, W. Xie, C. Ho, D. Bluemke and J. Noble, "Ω-Net (Omega-Net): Fully automatic, multi-view cardiac MR detection, orientation, and segmentation with deep neural networks," *Medical Image Analysis,* vol. 48, pp. 95-106, 2018.

[74] Z. Ma, X. Wu, X. Wang, Q. Song, Y. Yin, K. Cao, Y. Wang and J. Zhou, "An iterative multi-path fully convolutional neural network for automatic cardiac segmentation in cine MR images," *Medical Physics,* vol. 46, no. 12, pp. 5652-5665, 2019.

[75] M. Penso, S. Moccia, S. Scafuri, G. Muscogiuri, G. Pontone, M. Pepi and E. Caiani, "Automated left and right ventricular chamber segmentation in cardiac magnetic resonance images using dense fully convolutional neural network," *Computer Methods and Programs in Biomedicine,* vol. 204, 2021.

[76] S. Ghadimi, D. Auger, X. Feng, C. Sun, C. Meyer, K. Bilchick, J. Cao, A. Scott, J. Oshinski, D. Ennis and F. Epstein, "Fully-automated global and segmental strain analysis of DENSE cardiovascular magnetic resonance using deep learning for segmentation and phase unwrapping," *Journal of Cardiovascular Magnetic Resonance,* vol. 23, no. 20, 2021.

[77] J. Karr, M. Cohen, S. McQuiston, T. Poorsala and C. Malozzi, "Validation of a deep-learning semantic segmentation approach to fully automate MRI-based left-ventricular deformation analysis in cardiotoxicity," *British Journal of Radiology,* vol. 94, 2021.

[78] B. Spottiswoode, X. Zhong, C. Lorenz, B. Mayosi, E. Meintjes and F. Epstein, "Motion-guided segmentation for cine DENSE MRI," *Medical Image Analysis,* vol. 13, no. 1, pp. 105-115, 2009.

[79] The MathWorks, Inc, "alphaShape," 2014. [Online]. Available: https://www.mathworks.com/help/matlab/ref/alphashape.html. [Accessed 21 April 2021].

[80] The MathWorks, Inc, "Working with Delaunay Triangulations," 2021. [Online]. Available: www.mathworks.com/help/matlab/math/delaunay-triangulation.html. [Accessed 21 April 2021].

[81] P. A. Jones and J. S. Wilson, "The potential for quantifying regional distributions of radial and shear strain in the thoracic and abdominal aortic wall using spiral cine DENSE MRI," *J Biomech Eng,* vol. 143, no. 6, 2021.

[82] Z. Danziger, "Discrete Frechet Distance (version 1.4.0.0)," 2013. [Online]. Available: https://www.mathworks.com/matlabcentral/fileexchange/31922-discrete-frechet-distance. [Accessed 12 April 2021].

[83] T. Eiter, Mannila and Heikki, "Computing Discrete Frechet Distance," Christian Doppler Laboratory, Vienna University of Technology, Vienna, 1994.

[84] L. Pape, M. Awais, E. Woznicki, T. Suzuki, S. Trimarchi and A. Evangelista, "Presentation, Diagnosis, and Outcomes of Acute Aortic Dissection: 17-Year Trends From the International Registry of Acute Aortic Dissection," *Journal of the American College of Cardiology,* vol. 66, no. 4, pp. 350-358, 2015.

[85] G. C. Hughes, "Management of acute type B aortic dissection; ADSORB trial," *Endovascular Repair,* vol. 149, no. 2, pp. 158-162, 2015.

[86] L. Hiratzka, G. Bakris, J. Beckman, R. Bersin, V. Carr and D. Casey Jr., "2010 ACCF/AHA/AATS/ACR/ASA/SCA/SCAI/SIR/STS/SVM Guidelines for the Diagnosis and Management of Patients With Thoracic Aortic Disease," *Circulation,* vol. 121, no. 13, pp. 266-369, 2010.

[87] A. Evangelista, E. Isselbacher, E. Bossone, T. Gleason, M. Di Eusanio and U. Sechtem, "Insights from the international registry of acute aortic dissection," *Circulation,* vol. 137, no. 17, pp. 1846-1860, 2018.

[88] G. Kuzmik, A. Sang and J. Elefteriades, "Natural history of thoracic aortic aneurysms," *J Vasc Surg,* vol. 56, no. 2, pp. 565-571, 2012.

[89] A. de Wit, K. Vis and J. Richmond, "Aortic stiffness in heritable aortopathies: relationship to aneurysm growth rate," *Heart Lung and Circulation,* vol. 22, no. 1, pp. 3-11, 2012.

[90] X. Lu, J. Zhao, G. Wang, H. Gregersen and G. Kassab, "Remodeling of the zero-stress state of femoral arteries in response to flow overload," *Am J Physiol Heart Circ Physiol,* vol. 280, no. 4, pp. 1547-1559, 2001.

[91] M. Ramella, P. Bernardi, L. Fusaro, M. Manfredi, F. Casella and C. Porta, "Relevance of inflammation and matrix remodeling in abdominal aortic aneurysm (AAA) and popliteal artery aneurysm (PAA) progression," *American Journal of Translational Research,* vol. 10, no. 10, pp. 3265-3275, 2018.

[92] C. Collins and E. Tzima, "Hemodynamic forces in endothelial dysfunction and vascular aging," *Experimental Gerontology,* vol. 46, no. 2, pp. 185-188, 2011.

[93] M. Markl, W. Wallis and A. Harloff, "Reproducibility of flow and wall shear stress analysis using flow-sensitive four-dimensional MRI," *Journal of Magnetic Resonance Imaging,* vol. 33, pp. 988-994, 2011.

[94] R. van der Palen, A. Roest, P. van den Boogaard, A. de Roos, N. Blom and J. Westenberg, "Scan-rescan reproducibility of segmental aortic wall shear stress as assessed by phase-specific segmentation with 4D flow MRI in healthy volunteers," *Magnetic Resonance Materials in Physics, Biology and Medicine,* vol. 31, pp. 653-663, 2018.

[95] T. Suzuki, K. Eagle, E. Bossone, A. Ballotta, J. Froehlich and E. Isselbacher, "Medical management in type B aortic dissection," *Annals of Cardiothoracic Surgery,* vol. 3, no. 4, pp. 413-417, 2014.

[96] F. Mussa, J. Horton, R. Moridzadeh, J. Nicholson, S. Trimarchi and K. Eagle, "Acute aortic dissection and intramural hematoma: a systematic review," *JAMA,* vol. 316, no. 7, pp. 754-763, 2016.

Vita

Patrick Anderson Jones was born September 21st, 1996 in Fairfax, Virginia and grew up in South Riding, Virginia. He graduated from Freedom High School in South Riding, Virginia in 2015. After finishing high school, Patrick attended Virginia Commonwealth University in Richmond, Virginia to study Biomedical Engineering. As an undergraduate student, Patrick worked in the Orthopedic Research Laboratory studying musculoskeletal biomechanics, was involved in Greek life where he served as his fraternity's president, and volunteered as an EMT in Hanover County. Patrick graduated magna cum laude in May 2019 with a Bachelor of Science, earning University Honors from the VCU Honors College and the Gerald E. Miller Award for Academic Excellence from the Department of Biomedical Engineering. Following graduation, Patrick remained at Virginia Commonwealth University as a Master of Science student, conducting research under Dr. John Wilson in the Cardiovascular Mechanics and Imaging Laboratory. This summer, Patrick plans to continue his academic career by matriculating as an MD-PhD student at Emory University School of Medicine in Atlanta, Georgia.